Breakdown of Archard law due to transition of wear mechanism from plasticity to fracture

Jianqiao Hu [a,b], Hengxu Song [c*], Stefan Sandfeld [c,d], Xiaoming Liu [a,b*], Yueguang Wei [e]

[a] State Key Laboratory of Nonlinear Mechanics, Institute of Mechanics, Chinese Academy of Sciences, Beijing 100190, P R China

[b] School of Engineering Science, University of Chinese Academy of Sciences, Beijing 100049, P R China

[c] Institute for Advanced Simulation, IAS-9: Materials Data Science and Informatics, Forschungszentrum Juelich GmbH, Juelich 52425, Germany

[d] Faculty 5, RWTH Aachen University, 52062 Aachen, Germany

[e] Department of Mechanics and Engineering Science, College of Engineering, Peking University, Beijing 100871, P R China

[*]*Corresponding authors:* H.Song@fz-juelich.de, xiaomingliu@imech.ac.cn

Abstract:

Widely used to quantify material wear, the Archard wear law was derived from the asperity flattening model. However, the flattening model is so idealized that it cannot properly represent the real situation with general interlocked asperities, where asperity plowing dominates the wear instead of shearing flattened asperity. Using molecular dynamics simulations, we discussed if Archard law can hold during plowing wear of interlocked interface. Our results indicated Archard law breaks down when fracture dominates the wear. Furthermore, increasing interfacial adhesion or decreasing material ductility changes the dominant wear factor from plasticity to fracture. Finally, we proposed a criterion to determine when Archard wear law will break down and discussed the proposed criterion for real materials.

Keywords:

Archard wear law; Molecular dynamics; Asperity plowing; Dislocation plasticity; Fractured debris.

Nomenclature

a	lattice constant of FCC crystal
a_c	contact radius during flattening
d^*	critical junction size
F_z	normal force between asperities
G	shear modulus
H	material hardness
h	plowing depth
K_w	wear coefficient
k_0	specific wear rate
l_a	junction size of asperity plowing
l_x, l_y, l_z	substrate size
P	normal load between contact surfaces
R	radius of hemispherical asperity
r_c	cut-off radius for coarse-grained potentials
r_0	unit length for coarse-grained potentials
R_c, R_{MD}, R_{Exp}	critical asperity radius
t_0	unit of time
V_w	wear volume
V_a	volume of hemispherical asperity
α	normalized plowing depth, h/R
$\sigma_j, \sigma_{MD}, \sigma_{Exp}$	shear strength
η^{Mises}	atomic equivalent strain
Δw	surface energy
λ	adhesion ratio
λ_s	shape factor
ρ_{ini}	initial dislocation density
η_0, η_f	normalized area of new surface

1. Introduction

Material wear between surfaces in contact during relative sliding widely exists in modern industry. It was reported that 3% of the global energy consumption is used to remanufacture worn parts and spare equipment due to wear and wear-related failures [1]. Despite the importance of wear on energy saving and economic growth, our understanding of wear unfortunately still hovers around the famous Archard wear law which was proposed in 1953. According to the Archard law [2], the volume of the worn material dV is proportional to the normal load P and the sliding distance ds, and inversely proportional to the material hardness H: $dV = K_w Pds/H$ with K_w being the wear coefficient. The interpretation of the Archard wear law is based on the hypothesis of energy dissipation: Pds is proportional to the external work done by the friction force, and the dissipation through the plastic deformation is represented by H. A severe plastic deformation results in material wear.

The derivation of the Archard wear law is straightforward based on the flattened asperity model, as shown in Fig. 1(a). The asperity is plastically flattened by a normal load F_z, resulting in a contact radius of a_c. The normal load F_z can be calculated as $F_z = \pi a_c^2 H$. It is further assumed with the sliding distance $ds = 2a_c$, that the generated wear volume is proportional to the volume of a hemisphere of radius a_c: $dV = \gamma \frac{2}{3}\pi a_c^3$ where γ is a proportionality parameter. Therefore, the wear volume per unit sliding distance can be calculated as

$$\frac{dV}{ds} = \frac{\gamma \frac{2}{3}\pi a_c^3}{2a_c} = \frac{\gamma}{3}\pi a_c^2 = \frac{\gamma}{3}\frac{F_z}{H} = K_w \frac{F_z}{H}, \tag{1}$$

where K_w is known as the wear coefficient.

On the rough surface level, the total wear volume is the summation of the material wear at all asperities. Therefore for the macroscopic surface, the wear volume can be calculated by:

$$\frac{dV}{ds} = K_w \frac{\sum F_z}{H} = K_w \frac{P}{H}. \tag{2}$$

Here P is the total normal load on the surface.

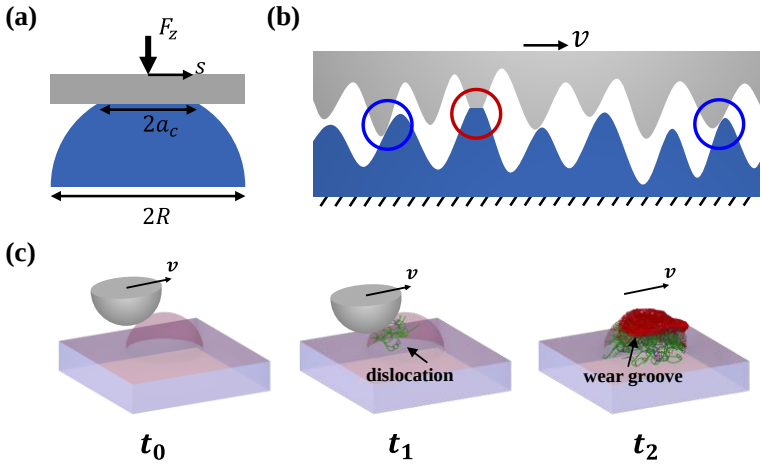

Fig. 1. (a) 2D schematic of the wear process based on the 3D flattened asperity model. The asperity is compressed by a normal load F_z and then sheared by a displacement of *s*. (b) Schematic of asperity configurations during the relative sliding between rough surfaces. Red circle highlights the flattened asperities, and blue circles highlight the plowing asperities. (c) Asperity configuration at different times during the asperity plowing process. Dislocations are shown at the time of t_1 and t_2; the red atoms at t_2 (the upper asperity is not shown) are worn atoms.

Although the Archard wear law has been widely used to quantify the material wear in tribological experiments [3-6], the direct confirmation of the flattened asperity model was not possible until the extensive studies of wear characteristics of atomic force microscopy tips, where the asperity fracture happens at certain circumstances [7, 8]. Recently, it has been shown through molecular dynamics (MD) simulations [9] that there exists a critical length scale that controls the formation of wear debris at the asperity level:

$$d^* = \lambda_s \cdot \frac{\Delta w}{(\sigma_j^2/G)}, \tag{3}$$

where G is the shear modulus and σ_j is the shear strength of the junction (the weaker one of the bulk material shear strength and the adhesion strength), Δw is the energy associated to newly created free surfaces, and λ_s is a shape factor. Junctions with size larger than d^* produce the fracture-induced debris while the smaller ones deform plastically. Recent MD studies by Zhao and Aghababaei [10, 11] simulated the wear between an asperity and a rigid platen (similar to the schematic in Fig. 1(a)); the simulation results confirmed the Reye wear law (the wear volume is linearly proportional to the work of frictional load) holds only when

the plastic deformation of the asperity dominates the wear. By performing a rigid flat tip sliding over a single asperity, Yang et al. [12, 13] studied material wear under different normal contact stresses: when the contact stress is small, material wear is caused by interfacial adhesion via atom-by-atom attrition; when the contact stress is large, material wear is caused by the plastic flow. In the above models, the role of adhesion seems to be overestimated because of their model setup: adhesion is necessary to transfer the shear loading; without adhesion, there will be essentially no wear in their models. In addition, these analyses based on the flattened asperity model cannot explain why the Archard wear law is commonly observed during the wear of real rough surfaces, as shown in Fig. 1(b). There, instead of the flattened asperity in the red circle, interlocking asperities in blue circles are more commonly seen. Therefore, it is crucial to confirm whether the Archard wear law still holds for the case of asperity plowing. Furthermore, most of the above numerical studies are carried out based on pristine crystals, while the initial defects greatly affect the plastic deformation at small scales [14]. Then, another issue arises how the initial defects affect asperity plowing and thus the Archard wear law.

In this paper, through MD simulations shown in Fig. 1(c), we try to address the question: Is the Archard wear law still satisfied for asperity plowing over a wide range of plowing conditions, including asperity size, plowing depth, and material ductility? First, using a series of model materials, we clarified when and how the Archard law breaks down in the plowing wear. Based on all case studies, we proposed a criterion for the transition of the wear mechanism. Then, the critical size for the transition is discussed in pristine crystals and crystals with initial defects for the model materials. In addition, the extension of our model is carried out for some real materials. Taking copper as an example, we clarified the role of adhesion on the material wear, which was not properly addressed in the flattened asperity models published previously [10, 11, 15]. The paper is organized as follows: Section 2 presents the MD modeling details and the definition of material wear at the atomic scale. In Section 3, we study the plowing wear and determine the wear condition for the breakdown of Archard law. The effect of initial dislocations on wear is also discussed. Section 4 further explores the plowing wear for several common materials, with the contact interface being both non-adhesive and adhesive. Finally, Section 5 summarizes our findings.

2. Model description and methodology

To understand the wear law for different materials at the asperity level, we performed MD simulations of the asperity plowing with a group of virtual materials characterized by coarse-grained potentials developed recently [9]. Compared to the conventional potentials used in the MD simulations, the modified coarse-grained potential (see Appendix A) has the advantage that the material's brittle/ductile property can be tuned without changing the elastic properties. This provides an opportunity to study the effect of material ductility on the wear process. In this study, all MD simulations are carried out by employing the Large-scale Atomic/Molecular Massively Parallel Simulator [16]. In this section, we first describe the model setup of asperity plowing and then introduce the definition of wear.

2.1 The model setup of asperity plowing

The plowing model contains two hemispherical asperities and a substrate, as shown in Fig. 2. The two asperities have the same radius of R, and the lower asperity is located at the center of the substrate. The lengths of the substrate in the x and y directions are the same (i.e., $l_x = l_y$), and the thickness in z direction is l_z. The dimensions of the substrate are listed in Table 1 for materials with coarse-grained potentials.

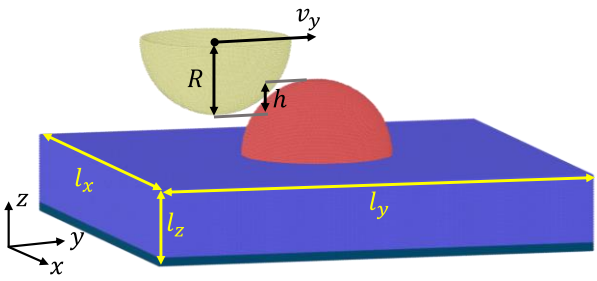

Fig. 2. Geometrical model of the asperity plowing.

For all simulations, the asperity and the substrate are all assumed with a face-centered cubic (FCC) structure. The upper hemispherical asperity is set to rigid, and the lower asperity and the substrate are deformable with the same material. The x, y, and z-axes of the lower asperity and the substrate are oriented in the [100], [010], and [001] lattice directions, respectively. Periodic boundary conditions are employed along the x and y directions, and the free boundary condition is adopted along the z direction. At the bottom of the substrate, atoms

with a thickness of $0.1R$ are fixed; other atoms in the lower asperity and substrate obey the classical Newton's second law. For all simulations, we defined the normalized plowing depth as $\alpha = h/R$. In the analysis, we used the dislocation extraction algorithm (DXA) [17] to track dislocations, and used the open-source software OVITO [18] to visualize the defects.

2.2 Simulation Parameters with modified potentials

Prior to the plowing, the model is first relaxed at a temperature of $0.005\varepsilon/k_B$ for $50t_0$ (k_B is the Boltzmann constant, and t_0 is the reduced time unit) to achieve the minimum energy. Then, at the plowing depth α, the upper rigid asperity moves along *y* direction at a constant velocity of $0.1a/t_0$. During the plowing, the temperature is enforced to $0.005\varepsilon/k_B$ using the Nose´-Hoover thermostat. In addition, the simulations of asperity wear were also performed at a lower plowing velocity ($0.05a/t_0$) and a higher temperature of $0.05\varepsilon/k_B$, and this alters the results only negligibly (see Supplementary Material). The parameters are summarized in Table 1.

Table 1 Parameters for asperity plowing with coarse-grained potentials.

Parameters	Values/expression
Deformable asperity radius	$R = 30a$, a (lattice constant)= $\sqrt{2}r_0$
Rigid asperity radius	$R = 30a$
Substrate size	$l_x = 6R$, $l_y = 6R$, $l_z = R$
Time step (t_0)	0.0025
Temperature (ε/k_B)	0.005
Plowing velocity (a/t_0)	0.1
Plowing depth (α)	0.1~0.6
Plowing direction	[010] on (001) surface

Using the plowing model with coarse-grained potentials, we studied the asperity wear in materials of different ductile properties. The effect of interfacial adhesion can be checked by changing the cohesion energy with an adhesion factor λ where a larger value of λ denotes

stronger interfacial adhesion. The potential used between the asperity pairs, if not explicitly stated, is the same as the one used within the lower asperity, indicating the interfacial strength between asperities is the same as the strength of the bulk asperity.

2.3 Definition of wear in asperity plowing

The conventional criterion to determine the "worn atoms" is based on a certain threshold of atomic position or velocity. For example, in the MD simulations of nano scratching on an atomistic flat surface, the worn atoms are evaluated as the atoms located above the original substrate surface [19] (which we term as the conventional wear criterion) or the atoms with velocities approaching the sliding velocity of the tip [20]. However, these methods cannot be used to define the worn atoms for asperity plowing due to the complex geometries and the large deformations. We utilize the atomic equivalent strain η^{Mises} [21] to define the worn atoms. The critical η^{Mises} is calibrated in the following way [22]: for given materials, we carried out nano-scratching simulations on a flat surface. The wear volume, which is calculated by multiplying the number of worn atoms and the volume of a single atom in a perfect crystal, is firstly evaluated by the conventional wear criterion, then the wear volume is evaluated again using the atomic equivalent strain criterion to determine the critical η^{Mises}.

For example, for copper, we calibrated the critical η^{Mises} to be 1.5. The critical η^{Mises} is not a universal value, therefore, for new 'materials', this calibration needs to be repeated. The details of the calibration can be found in Appendix B. For cases with coarse-grained potentials, we utilized the same method to determine the threshold strain for worn atoms. The result showed that the threshold strain is different when the material's ductility varies (details can be found in Appendix B). Furthermore, we found that the atomic strain criterion can describe the worn atoms only when plasticity dominates the asperity wear and it becomes invalid for fracture-induced wear debris. Because of this limitation, we combined the wear criterion that has been used in the adhesive plowing model [23, 24]: the atoms removed from the lower asperity are also considered as worn atoms. As a result, the atoms with atomic equivalent strain larger than the critical η^{Mises} and the atoms removed from the lower asperity are considered as worn atoms in our simulations.

3. Breakdown of Archard law due to asperity fracture

In order to see whether the Archard wear law holds for different materials, we utilized the coarse-grained interatomic potentials developed by Aghababaei et al. [9] to perform the plowing simulations. Details of the interatomic potentials can be found in Appendix A. Basically, the cut-off radius r_c in Eq. (9) controls the material ductility. The case with $r_c = 1.22r_0$ characterizes a brittle material while another case with $r_c = 1.38r_0$ describes a ductile material.

3.1 Plowing wear of single asperity

In a scratch of single asperity, the increase of the normal load would lead to a larger plowing depth. Here, we first quantified the wear for different plowing depths during the adhesive plowing in materials of $r_c = 1.22r_0$. Fig. 3(a) shows the evolution of the wear volume with the increasing plowing distance at different plowing depths. For one plowing depth, the wear volume initially increases with the increasing plowing distance, then saturates. We take the wear volume when the plowing is finished as the final wear volume. When the plowing depth exceeds 0.4, the final wear volume does not always increase. This is due to the transition of the wear mechanism from plasticity to fracture when the plowing depth is larger than ~0.4. To determine whether the plowing wear is dominated by plasticity smoothing or fractured wear debris, we developed a criterion based on the formation of free surface to identify the wear mechanism (see Appendix C).

Fig. 3(b) illustrates the atomic strain with two plowing depths at the end of plowing. For the plowing depth of $\alpha = 0.1$, the asperity tip is chopped and flattened, i.e., asperity smoothing takes place. In this situation, only a few worn atoms are generated. Correspondingly, very few dislocations are left in the asperity, as shown in Fig. 3(c). By analyzing the dislocation structures during plowing, we confirmed that dislocations initially nucleate at the contact region; however, the nucleated dislocations finally annihilate at the free surface of asperity due to image forces. In contrast, for the large plowing depth of $\alpha = 0.5$, the asperity is fractured to form irregular debris. At the same time, numerous dislocations are generated during plowing (see Fig. 3(c)). The asperity deformation associated with these dislocation activities can be seen in Fig. 3(b),

where atomic strain larger than the defined strain criterion ($\eta^{\mathrm{Mises}} \geq 6.0$) can be found with a large volume. Also, we noticed that some atoms removed from the lower asperity have atomic strain less than the critical value. However, these atoms are also considered as worn atoms and contribute to the wear volume in Fig. 3(a).

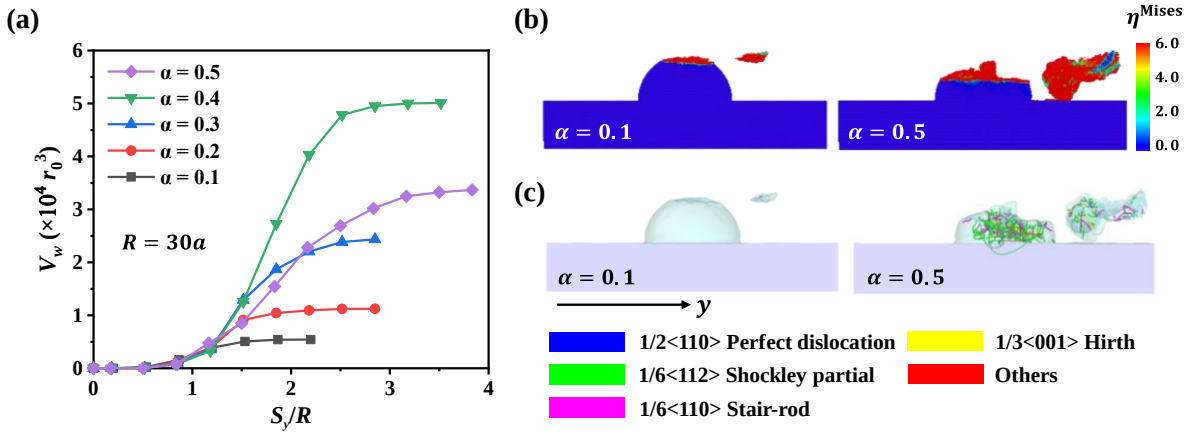

Fig. 3. (a) Evolution of wear volume with increasing plowing distance in asperity with radius of 30a. (b) Distribution of atomic equivalent strain and (c) dislocation structures at the time when the plowing is finished. The upper rigid asperity is not shown.

3.2 Breakdown of Archard law in brittle asperity

In our simulation, we can rewrite the Archard wear law as

$$V_w = \int dV = K_w v_y \int F_z/H \cdot dt. \quad (4)$$

Here, V_w and v_y are the wear volume and the sliding velocity, respectively. We introduced a parameter E_z to consider the combined effect of the normal load and the plowing distance at the asperity level, $E_z = v_y \int F_z \cdot dt$. By flattening asperities of different sizes, we found that the flatten hardness H is almost size independent for asperity with radius ranging from 20a to 40a (see Supplementary Material); therefore, we can further rewrite Eq.(4) as

$$V_w = k_0 E_z. \quad (5)$$

Here, $k_0 = K_w/H$ is the so-called specific wear rate [25].

By analyzing the plowing wear in materials of different ductility, we found that Archard law holds for ductile material but breaks for brittle material. Fig. 4(a) summarized the results of adhesive plowing for materials of different ductility in terms of Eq. (5). For the ductile materials ($r_c = 1.30r_0$ and $r_c = 1.38r_0$), good linearity can be observed for asperity wear and

k_0 is roughly a constant. Therefore, the Archard wear law remains valid. Correspondingly, the dominant wear mechanism for ductile asperities at the plowing depth of 0.5 is plastic smoothing rather than fractured wear debris, as shown in Fig. 4(b). In contrast, for the brittle material ($r_c = 1.22r_0$), the Archard law is satisfied only at a smaller value of E_z which corresponds to the shallow plowing depth. However, for brittle asperity at the plowing depth of 0.5 (see Fig. 3), the fracture-induced wear debris forms, thus breaking the Archard wear law.

In addition to the material ductility, interfacial adhesion may also play a vital role in the validity of Archard law. As shown in Fig. 4(a), when the adhesion strength is reduced to $\lambda = 0.6$, the Archard wear law is recovered even at the larger plowing depth. The corresponding wear morphology (last row of Fig. 4(b)) becomes asperity smoothing, i.e., for weak adhesion, the fracture-induced debris won't form. We also studied the non-adhesive plowing for materials of different ductility; it is concluded that Archard law always holds because the dominant wear mechanism is plasticity which is exactly the fundamental assumption of Archard law.

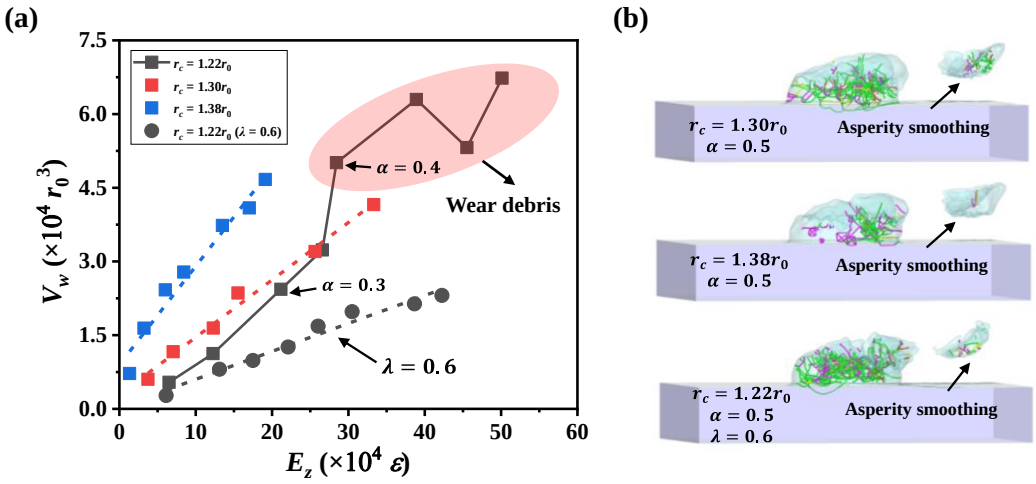

Fig. 4. (a) Wear volume as the function of E_z in asperity of radius 30a. (b) Dislocation structures in asperity with different plowing conditions.

3.3 A model to determine the breakdown of Archard law

From the above results and analysis, we can conclude that the failure of the Archard wear law is attributed to the transition of the wear mechanism from the plasticity-induced asperity smoothing to the fracture-induced wear debris. The question of when this transition happens for a given asperity remains elusive. For plowing asperities, the question essentially includes

two aspects: how large the asperity has to be, and how deep the plowing depth should be to generate the fracture-induced debris to fail the Archard wear law.

In the plowing model of a hemisphere of radius R and plowing depth α, the junction size during the plowing process can be estimated as $l_a = \sqrt{4\alpha - \alpha^2}R$ based on geometric analysis. Particularly, $l_a^{max} = \sqrt{3}R$ by assuming the maximum depth $\alpha = 1.0$. From Eq. (3), the minimum junction size to form fracture is $d^* = \lambda_s \cdot \frac{\Delta w}{(\sigma_j^2/G)}$. By combining l_a and d^*, the plowing depth α to form fracture can be derived as $2 - \sqrt{4 - \left(\frac{d^*}{R}\right)^2}$.

Furthermore, we proposed a critical asperity size by combining the expressions of l_a^{max} and d^*, and the critical size can be expressed by:

$$R_c = \frac{\lambda_s}{\sqrt{3}} \cdot \frac{\Delta w}{(\sigma_j^2/G)}. \quad (6)$$

When the asperity size R is smaller than R_c, the Archard wear law always holds. This is because the wear is controlled by plastic deformation independent of the plowing depths. When the asperity size R is larger than R_c, the Archard wear law will hold only when the plowing depth satisfies $\alpha < 2 - \sqrt{4 - \left(\frac{d^*}{R}\right)^2}$. In Eq.(6), σ_j is the smaller value between the interfacial strength and the asperity yield strength (or the apparent yield strength due to the combination of decohesion and plasticity, as discussed in [26]), this fact indicates that R_c will be a large value for non-adhesive plowing (σ_j is very small for non-adhesive case). Note that this critical size is proposed based on the assumption that the two asperities have the same radius. For two plowing asperities with different radii, the geometric analysis would yield a different result, but the fundamental findings still hold that the Archard wear law breaks down due to the formation of fractured wear debris.

Based on the above analysis, we now reinterpret our simulation results. For the brittle material with $r_c = 1.22r_0$, the critical junction size d^* is $43 \pm 9r_0$ based on the shear strength determined by flattening (see Supplementary Material), which is consistent with $50r_0$ in [27]. For the critical junction size of $50r_0$, the corresponding critical radius R_c is around $29r_0$ from Eq.(6). When the asperity size R is $30a$ with $a = \sqrt{2}r_0$, the critical plowing depth $\alpha = \sim 0.38$. Our simulation results (see Fig. 4(a)) are consistent with this analytical prediction that the wear mechanism is the asperity smoothing when the plowing depth is 0.3, and becomes

fracture-induced debris as the depth increases to 0.4.

Fig. 5 further confirms the breakdown of the linear wear law due to the wear mechanism changing to fracture-dominated. Fig. 5(a) shows the wear volume as a function of E_z for asperity with the radius of $20a$ over a wide range of plowing depths α from 0.1 to 0.5; the linearity shows clear Archard law, and microstructure analysis indicates a consistent finding of the plasticity-induced asperity smoothing. Because the asperity size is less than R_c (~$29r_0$) from Eq.(6), the asperity wear is dominated by plasticity, so the Archard wear law remains valid. While in another example of Fig. 5(b), for asperity with the radius of $40a$ (larger than R_c), the transition of wear mechanism occurs as the plowing depth increases to 0.4. With plowing depth α larger than 0.4, the Archard wear law breaks down.

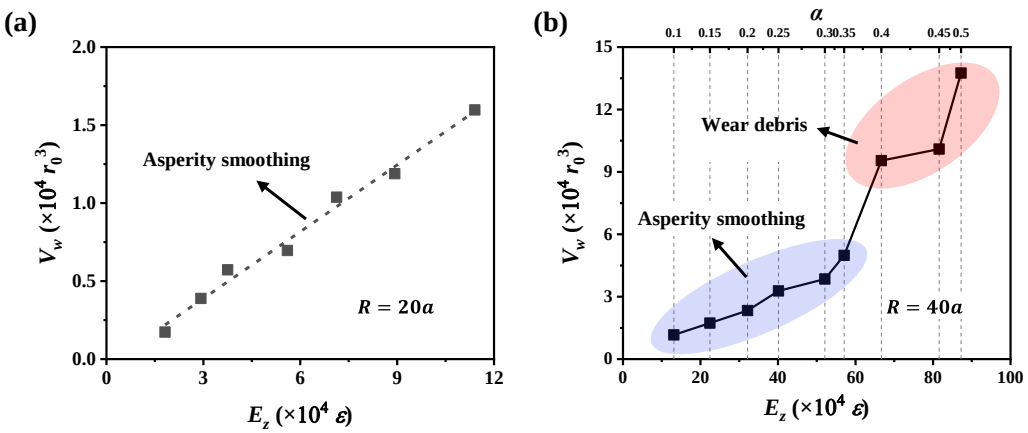

Fig. 5. Wear volume as a function of E_z in asperity with (a) $R = 20a$, and (b) $R = 40a$ in material of $r_c = 1.22r_0$. The plowing depths are also shown for asperity with radius of $40a$.

Furthermore, the effect of the reduced adhesion in Fig. 4 can be well understood: when the interfacial adhesion is reduced by $\lambda = 0.6$, R_c is calculated to be ~$80r_0$ from Eq.(6), while the asperity size is $30\sqrt{2}r_0$ in the simulations. Therefore, asperity wear is dominated by plasticity, and the Archard wear law still holds. For $r_c = 1.30r_0$ and $r_c = 1.38r_0$, R_c is ~$59r_0$ and ~$113r_0$ respectively; therefore, if the asperity size $30\sqrt{2}r_0$ less than R_c is used in our simulations, the Archard wear law should always hold.

3.4 Increased critical size due to initial dislocations

The above analysis for plowing wear is all based on pristine asperity with no initial defects. However, for actual materials, initial defects widely exist. In this section, we further studied the

plowing wear in asperities with initial defects.

The initial defects in the asperity are prepared by the following. The pristine asperity is first stretched along the *x* and *y* directions to a certain strain and then released to the state with no external load. By applying different strain magnitudes, we can get asperities with dislocations of different densities, as shown in Fig. 6(a). It was found that the wear mechanism tends to become the plasticity-induced asperity smoothing with increasing initial dislocation density. As shown in Fig. 6(b), for brittle asperity with a low dislocation density of $0.002r_0^{-2}$, the debris embryo forms due to the formation of crack. However, these cracks do not propagate and combine to form individual debris, so the plowing wear is still considered to be dominated by plasticity. In contrast, for asperity with initial dislocation density higher than $0.008r_0^{-2}$, the deformation becomes smoother without crack formation during plowing.

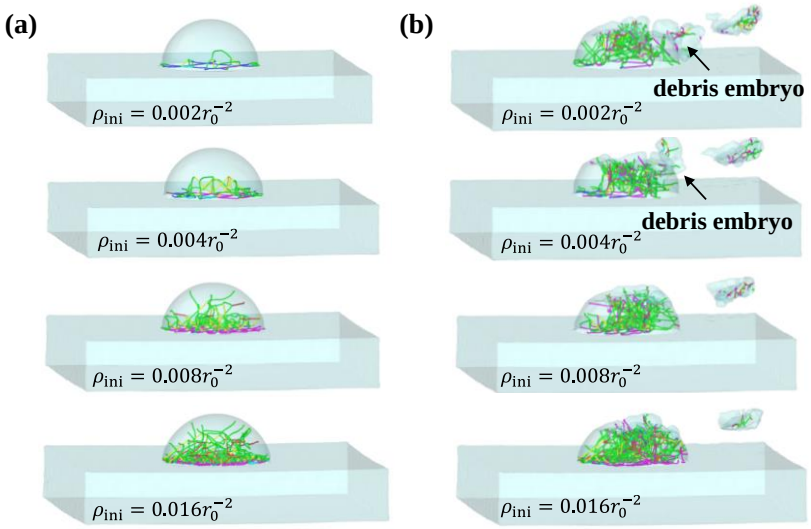

Fig. 6. Transition of wear mechanism in brittle asperity ($r_c = 1.22r_0$) with initial dislocations. (a) Initial dislocations in asperities, and (b) dislocation structures at the time when the plowing is finished. The plowing depth is 0.4.

Due to the existence of initial dislocations, the material becomes more ductile and thus leads to a larger critical size for the transition of wear mechanism. For asperity with initial dislocations, we first determined the shear strength by flattening the asperity (see Supplementary Material) and then obtained the critical size based on the analytical model in section 3.3. The simulation results are consistent with the analytical model that the dominant wear mechanism changes to the fractured wear debris when the plowing depth exceeds ~0.5, as

shown in Fig. 7.

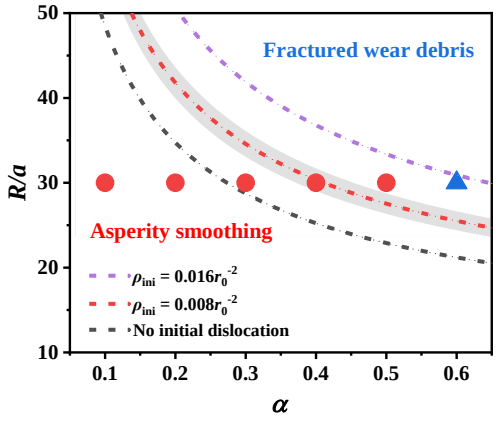

Fig. 7. The transition of wear mechanism due to the existence of initial dislocations. The dash lines are obtained by the analytical model, and the red dots are simulation results for asperity with $\rho_{ini} = 0.008r_0^{-2}$. The red shaded region for the case of $\rho_{ini} = 0.008r_0^{-2}$ corresponds to the variation of shear strength.

4. Archard wear law for real materials

From the above analysis, it can be seen that the Archard wear law breaks down as the wear mechanism changes from plasticity-induced asperity smoothing to fractured wear debris. In this section, the critical size for the transition of wear mechanism is further discussed for some real materials. Taking copper as an example, we carried out MD simulations for plowing copper asperity with EAM potential to check the Archard wear law. What is more, the non-adhesion plowing is discussed as a special case for copper asperity.

4.1 Critical size for the transition of wear mechanism

Using Eq. (6), we can roughly estimate the critical asperity size R_c below which the plasticity dominates the asperity wear. As shown in Table 2, we estimated six materials of different ductility and calculated their critical size for the transition of the wear mechanism. The material properties, including the surface energy and the shear modulus, are obtained from the literature of the potential function [28-30]. In the estimation, the surface energy is calculated on the (100) surface for Si with the diamond crystal (DC) structure, and the experimental average surface energy [29] was used for the FCC crystals. We used C_{44} in the fourth-order

elastic moduli as the shear modulus. The critical asperity radius for the wear transition in each material was discussed based on two sets of shear strength. First, for pristine crystals, i.e., no initial defects exist, the shear strength σ_{MD} is obtained through $\sigma_{MD} = \frac{1}{3\sqrt{3}}H$, where H is the material hardness determined by the indentation simulation using the similar way in Appendix A. All the indentations are performed on the (001) surface with a temperature of 300 K and an indentation velocity of 10 m/s. Second, the shear strength σ_{exp} for each material is also taken from their experimental measurements of open literature [31-36]. The two sets of shear strength differ greatly, on the one hand, because the indentation simulation starts with a pristine crystal, while for materials with initial defects [14, 37, 38], the yield stress is much lower; on the other hand, the indenter size used in MD is usually very small, and the calculated hardness has strong indentation size effect [39]. Based on the above two sets of shear strength, we can calculate the corresponding critical asperity radius, i.e., R_{MD} and R_{Exp} in Table 2. These two critical radii are also compared in Fig. 8.

Table 2 Predicting the critical asperity size for six typical materials.

Material	Cu	Au	Ni	Pd	Pt	Si
Lattice constant (Å)	3.615	4.08	3.52	3.89	3.92	5.431
Shear modulus (GPa)	76.2	45	128	65	68	56.4
Surface energy (mJ/m^2)	1790	1500	2380	2000	2490	2356
Crystal structure	FCC	FCC	FCC	FCC	FCC	DC
Shear strength, σ_{MD} (GPa)	1.622	0.913	2.428	1.245	1.329	2.209
Critical asperity radius, R_{MD} (nm)	179.6	280.5	179.0	290.5	332.1	94.5
Shear strength, σ_{Exp} (GPa)	0.1~0.5	0.13~0.25	0.1~0.6	0.25~0.6	~0.65	2.0~4.0
Critical asperity radius, R_{Exp} (10^3 nm)	1.9~47.2	3.7~13.8	2.9~105.5	1.3~7.2	~1.4	0.03~0.12

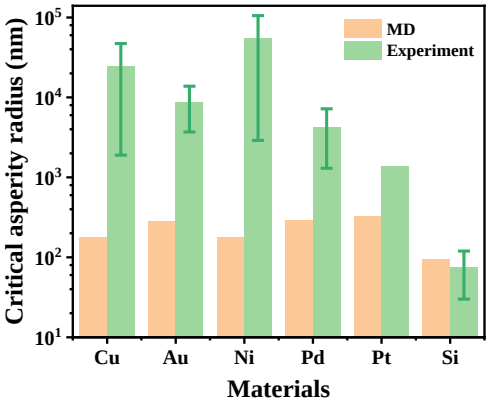

Fig. 8. The critical asperity size for the transition of wear mechanism in six typical materials. The experimental predictions are calculated based on the strength of Cu [31], Au [32], Ni [33], Pd [34], Pt [35], and Si [36].

From Table 2 and Fig. 8, it can be seen for pristine crystals, the critical asperity size R_{MD} is around a hundred nanometers for Si and a few hundred nanometers for other ductile metals. Experimentally, in the wear of Si atomic force microscopy (AFM) probes, the formation of wear debris was observed as the asperity size is larger than 100 nm [8]. However, these length scales are beyond the dimensions that MD simulations can handle; therefore, even for brittle materials such as Si, the plastic deformation rather than the formation of the fractured debris was widely observed in MD simulations of the wear process [40, 41].

The simple estimation based on the pristine crystals matches the wear process at a very small scale (below 100 nanometers) where materials could be assumed to be pristine. However, at the larger length scale, initial defects in the material, here we only consider initial dislocation microstructures, have a great influence on the material strength, therefore 'redefine' the critical asperity size. This is more likely to be the case in the real material, thus we estimated the critical asperity size based on the experimentally measured material strength. It can be seen from Fig. 8 that the critical asperity size R_{Exp} for ductile materials ranges from several micron meters to hundred micron meters. These length scales essentially imply that plastic deformation dominates the wear process in the rough surface, i.e., Archard wear law holds, because the fractured debris forms in asperity of the size of micron meters which is normally larger than the roughness of the material, i.e., there won't be a perfect asperity of this size on the rough surface.

In contrast, for Si, with the initial defects considered, the critical length scale can be even smaller than the estimation of its pristine counterpart, i.e., fractured debris may be in fact even easier to form.

The above discussion highlights the fact that even though Eq. (6) gives an estimation of the critical asperity size, the material strength involved in the estimation is much more complex than it seems. Any direct application/extension of Eq. (6) to the rough surface wear should be taken with special care. The initial dislocation microstructures [42, 43], the surface topology [44], and the material deformation history [45] all have a huge influence on the material yield strength.

4.2 Discussion on plowing wear of copper as an example

From the above discussion on critical size in real materials, we can expect that for the plowing wear of copper in MD simulations, the Archard wear law always holds because of the size constraints for MD simulations. In this section, as an example, we revisited the validity of the Archard wear law in copper asperity with both non-adhesive and adhesive plowing.

4.2.1 Parameters for plowing of copper asperity

Similar to the plowing of asperity with modified Morse potentials, the copper model with more real potential (EAM) is relaxed at a temperature of 0.01 K for a time span of 150 ps (in total 10^5 time steps) to achieve the minimum energy. Subsequently, the upper rigid asperity moves along the *y* direction at a constant velocity of 36 m/s (which corresponds to 0.1*a*/ps with *a* being the lattice constant). During plowing, the Nose´-Hoover thermostat was adopted to keep the active atoms at the temperature of 0.01 K. To study the size effect, the radius of the copper asperity varies from 5*a* to 50*a* where *a* is the lattice constant. The above parameters are also summarized in Table 3.

Table 3 Parameters used in the plowing of copper asperity.

Parameters	Values/expression
Deformable asperity radius	R = 5a~50a; a (lattice constant) = 3.615 Å

Rigid asperity radius	The same as the deformable asperity
Substrate size (repulsive potential)	l_x = 4R, l_y = 4R, l_z = 0.8R
Substrate size (Morse potential)	l_x = 6R, l_y = 6R, l_z = 0.8R
Time step (ps)	0.0015
Temperature (K)	0.01
Plowing velocity (m/s)	36
Plowing depth (α)	0.1~0.8
Plowing direction	[010] on (001) surface

The embedded atom method (EAM) potential [28] is adopted to describe the interactions among copper atoms. We use two types of interaction between asperity pairs to simulate the non-adhesive and adhesive plowing. First, for non-adhesive plowing, the interaction between the asperity pairs is simulated by a repulsive potential with a force of magnitude

$$F_i = \begin{cases} -K(r_i - R)^2, & \text{if } r_i \le R \\ 0, & \text{otherwise} \end{cases}. \quad (7)$$

Here, K is the effective stiffness and set to 10 eV/Å^3 in the simulation. r_i is the distance from the i^{th} atom to the center of rigid asperity. This interaction describes the non-adhesive contact at the interface. Second, for adhesive plowing, the upper asperity was fabricated as a diamond tip which comprises perfect diamond atomic lattices. In the diamond-copper system, the C-C interactions among atoms in the upper asperity are ignored because diamond is much harder than copper. The interaction between asperity pairs is described by the Morse potential as

$$\phi(r) = D_0\left[e^{-2\alpha_0(r-r_0)} - 2e^{-\alpha_0(r-r_0)}\right], \quad (8)$$

where D_0 is cohesion energy, α_0 is elastic modulus, r is the distance between two atoms, and r_0 is the equilibrium distance. Here, these parameters are taken as $D_0 = 0.087$ eV, $\alpha_0 = 5.14$ Å^{-1}, and r_0 = 2.05 Å [46]. To study the effect of interfacial adhesion, we use a factor λ to modify the cohesion energy by $\lambda \cdot D_0$, resulting in different adhesion strengths.

4.2.2 Size independence of plowing wear

Fig. 9(a) presents the effect of asperity size on the final wear volume and the normalized

wear volume V_w/V_a, where V_a is the volume of the undeformed hemispherical asperity and calculated as $2\pi R^3/3$. For the asperity of radius 5a, both the absolute and normalized wear volumes are small due to the limited plastic deformation. For the asperity of radius larger than ~20a, the normalized wear volume exhibits a weak dependence on the asperity size. Therefore, the wear volume can be considered to be proportional to the asperity volume in this case. Fig. 9(b) further confirms the size insensitivity of the normalized wear volume over a wide range of plowing depths for the asperities of radii 20a and 30a.

The distribution of atomic strain for asperities of different sizes is shown in Fig. 9(c); the three asperities are rescaled to have the same dimension in the picture. For the small asperity of radius 10a, only a limited number of atoms at the very top of the asperity are worn. In contrast, for the larger asperities, all atoms on the top region of the asperity are worn, and it is seen that the spatial locations of the worn atoms are almost independent of the asperity size.

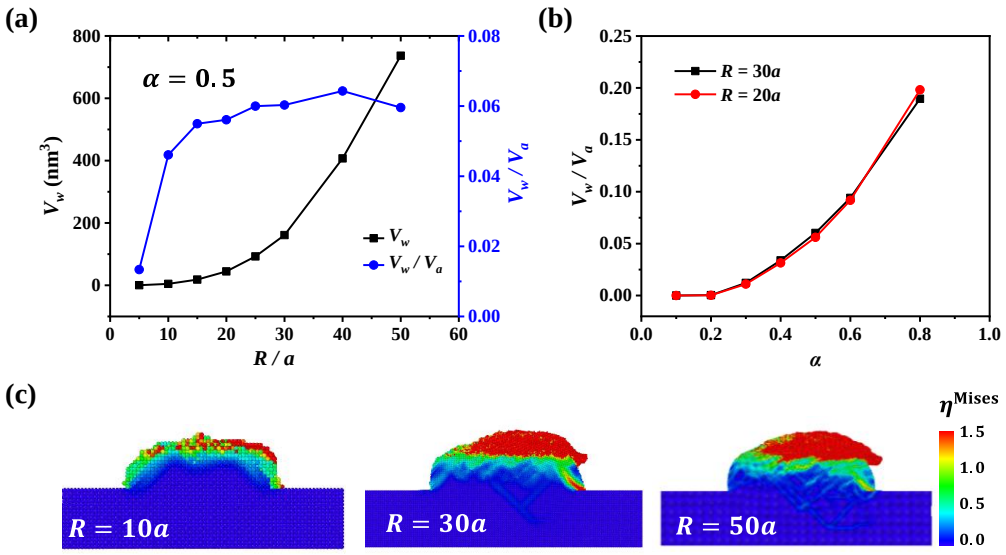

Fig. 9. (a) Effect of the asperity size on the wear volume when $\alpha = 0.5$. (b) The normalized wear volume for two asperities. (c) Distribution of the atomic equivalent strain in the asperity of different sizes when $\alpha = 0.5$. Figures are the cross section of the asperity.

4.2.3 Increased wear rate due to stronger adhesion

The results of non-adhesive plowing for copper asperity of various radii, in terms of Eq. (5), are summarized in Fig. 10. Good linearity can be observed, i.e., k_0 is roughly a constant. Therefore, the Archard wear law is confirmed to be valid for the non-adhesive asperity plowing.

This finding is different from the adhesive wear model due to the flattening and shearing of asperities [10], in which the adhesion is necessary to generate shear loading and then produces asperity wear by plastic deformation. In our model, we confirmed that the Archard wear law still holds in the absence of adhesion.

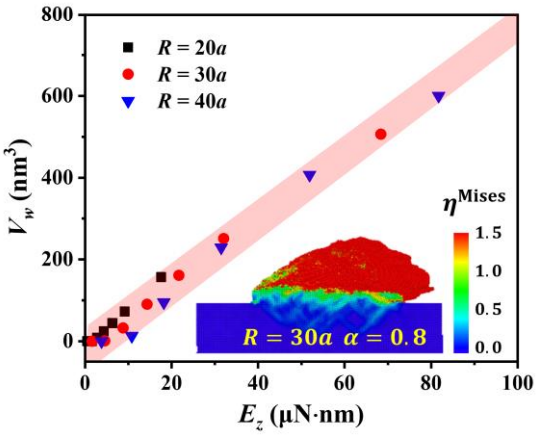

Fig. 10. Wear volume as a function of E_z with k_0 being 7.3 nm^3/(μN·nm). The inset shows the distribution of atomic equivalent strain when $\alpha = 0.8$. The pink shaded region is used to guide the readers for linearity.

For adhesive plowing in the diamond-copper system, the wear law is studied in the asperity of radius $30a$ with two adhesion strengths, i.e., the full adhesion ($\lambda = 1.0$) and the reduced adhesion by $\lambda = 0.5$. As shown in Fig. 11, two clear features can be observed. First, the Archard wear law holds in the adhesive plowing. Second, increasing the adhesion strength results in a higher wear rate k_0. In the insets of Fig. 11, we can see that a small amount of wear is attached to the rigid tip in the case of full adhesion. In contrast, when the adhesion strength is reduced, no debris is attached to the tip. Despite the difference, the wear processes with and without adhesion discussed above can be attributed to the same wear mechanism: wear is essentially dominated by plasticity-induced asperity smoothing [9]. In this situation, the Archard law always holds for copper.

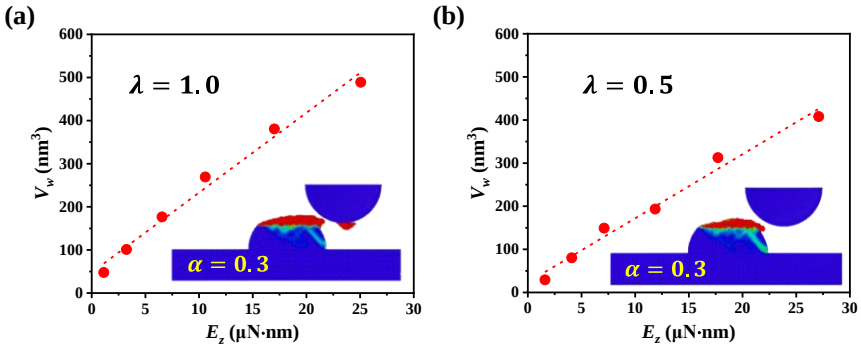

Fig. 11. Wear volume as a function of E_z: (a) full adhesion ($\lambda = 1.0$) with k_0 being 18.5 nm^3/(μN·nm); (b) $\lambda = 0.5$ with k_0 being 14.8 nm^3/(μN·nm). The inset shows the strain distribution following the color scheme in Fig. 10.

5. Conclusions

In this paper, through MD simulations of plowing wear in asperities using coarse-grained interatomic potentials and real material potentials, we addressed the fundamental question: whether Archard wear law holds for interlocking asperities. The main findings are summarized as follows:

1) There exists a critical asperity size below which the wear is dominated by the plastic deformation, and thus Archard wear law holds. The Archard wear law breaks down when the wear is dominated by the formation of fractured debris during plowing.

2) Increasing the material ductility or decreasing the interfacial adhesion makes the wear mechanism easier to transform from fracture-induced debris to plasticity-induced smoothing. Increasing initial dislocations may lead to a larger critical size of asperity due to the increased ductility.

3) An equation of the critical asperity size for the formation of fractured debris is proposed. The critical asperity size is estimated to be on the length scale of hundred nanometers for pristine crystals and several micron meters to hundred micron meters for crystals with initial defects. For ductile materials like copper, we confirmed by MD simulation that the Archard wear law maintains validity in both non-adhesive and adhesive plowing.

Appendix A: Coarse-grained interatomic potentials

This appendix introduced the coarse-grained interatomic potentials. As mentioned in [9],

the material ductility can be modified by changing the tail of a Morse potential. In detail, the modified Morse potentials are developed as follows:

$$\frac{E(r)}{\varepsilon} = \begin{cases} e^{-2\alpha_0(r-r_0)} - 2e^{-\alpha_0(r-r_0)} & r < 1.1r_0 \\ a_3r^3 + a_2r^2 + a_1r^1 + a_0 & 1.1r_0 \le r < r_c \\ 0 & r_c \le r \end{cases}. \quad (9)$$

Here, $E(r)$ is the potential energy between two atoms with distance r. ε is the depth of the potential well and is 1.0, and r_0 is the equilibrium bond distance. α_0 governs the bond stiffness and is equal to $7.3r_0^{-1}$. The truncation at $1.1r_0$ ensures the elastic properties unchanged up to 10% strain. The r_c is a parameter that governs the tail of interatomic potentials and then controls the unstable stacking fault energy. The parameters $a_0 \sim a_3$ ensure the continuity of the bond energy and the force.

In this study, we constructed three sets of potentials, as shown in Fig. A1(a). The potential with a shorter cut-off radius ($r_c = 1.22r_0$) corresponds to a more brittle material. In contrast, the increase of cut-off radius (e.g., $r_c = 1.38r_0$) makes the material more ductile. Therefore, using these model potentials, we essentially studied the wear law in different material systems. All the models with modified Morse potentials are constructed in the FCC structure with the lattice constant a being $\sqrt{2}r_0$. The Young's modulus for all materials is $150\varepsilon r_0^{-3}$ [27]. The indentation is simulated at the temperature of $0.005\,\varepsilon/k_B$ for materials with the modified Morse potentials, and the results are shown in Fig. C1(b). The material hardness is calculated by averaging the contact stresses at the normalized indentation depth between 0.3 and 0.4. More details for the hardness of indentation and flattening are given in the Supplementary Material. Generally, a more brittle material has a larger hardness in this model.

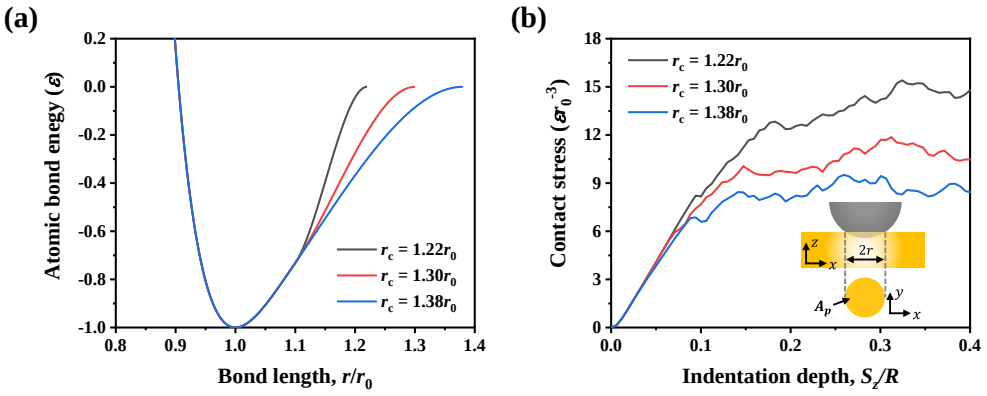

Fig. A1. (a) The bond energy versus atomic bond length for different cut-off radius r_c. (b)

Contact stress for materials with potentials of different r_c; the inset shows the indentation model with an indenter of radius 30a.

Appendix B: Determination of wear volume

In this appendix, we proposed a new method to evaluate the wear volume during asperity plowing. Nano-scratching simulations on an atomically smooth copper substrate are carried out as the benchmark. The nano-scratching model consists of a rigid indenter with a radius of 5 nm and a copper substrate of dimensions $\sim 30 \times 30 \times 10$ nm^3, see inset in Fig. A1. We used the same repulsive potential (Eq. (7)) as in the simulation of non-adhesive plowing to describe the interaction between the indenter and the substrate. The simple geometry in this model allows us to utilize a simple conventional criterion/definition of worn atoms: atoms on the top of the original substrate surface. The wear volume evaluated by the simple conventional criterion serves as a reference for developing the new wear criterion using the atomic equivalent strain η^{Mises} [21]. The atomic equivalent strain η^{Mises} is defined as

$$\eta^{\mathrm{Mises}} = \sqrt{\eta_{yz}^2 + \eta_{xz}^2 + \eta_{xy}^2 + \frac{(\eta_{yy}-\eta_{zz})^2+(\eta_{xx}-\eta_{zz})^2+(\eta_{xx}-\eta_{yy})^2}{6}}, \quad (10)$$

where η_{ij} is the component the strain tensor defined as $\boldsymbol{\eta} = \frac{1}{2}(\boldsymbol{JJ^T} - \boldsymbol{I})$, $\boldsymbol{J}$ is the local deformation gradient which is calculated based on the reference atomic configuration at the initial moment of sliding, and $\boldsymbol{I}$ is the unit tensor.

As shown in Fig. B1, we first obtain the worn atoms by the conventional criterion in two different scratching depths; in both cases, the wear volume increases with the increasing scratching distance. We then calculate the volume of the worn atoms using different atomic equivalent strains as the threshold. By comparing the wear volume defined by the two methods, the atomic equivalent strain of 1.5 is calibrated as the criterion of worn atoms. For nano scratching using a hemispherical diamond tip on the copper substrate where adhesion exists, we repeated the above calibration process, and it was found that the atomic equivalent strain of 1.5 is also the threshold strain.

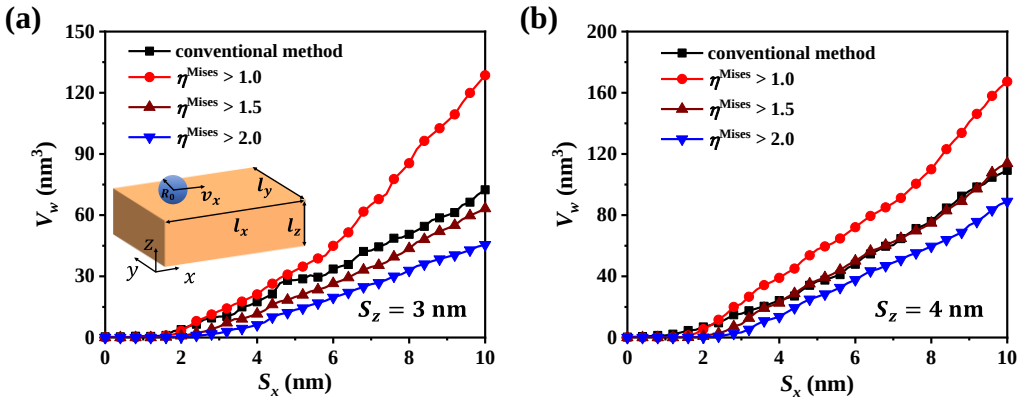

Fig. B1. Evaluation of the wear volume using different atomic equivalent strains as the threshold when the scratching depths are (a) $S_z = 3$ nm and (b) $S_z = 4$ nm. The inset in (a) illustrates the nano-scratching model.

Using the above method, we can also determine the wear criterion for the materials of coarse-grained potentials. We evaluated the wear volume at two scratching depths and determined the threshold strain for each potential, and the results for the material of $r_c = 1.38r_0$ are shown in Fig. B2. The threshold strains for the worn atoms are 6.0, 4.0, and 3.0 for the materials of $r_c = 1.22r_0$, $r_c = 1.30r_0$, and $r_c = 1.38r_0$, respectively. It can be seen that the calibrated threshold strains are different for materials of different ductility.

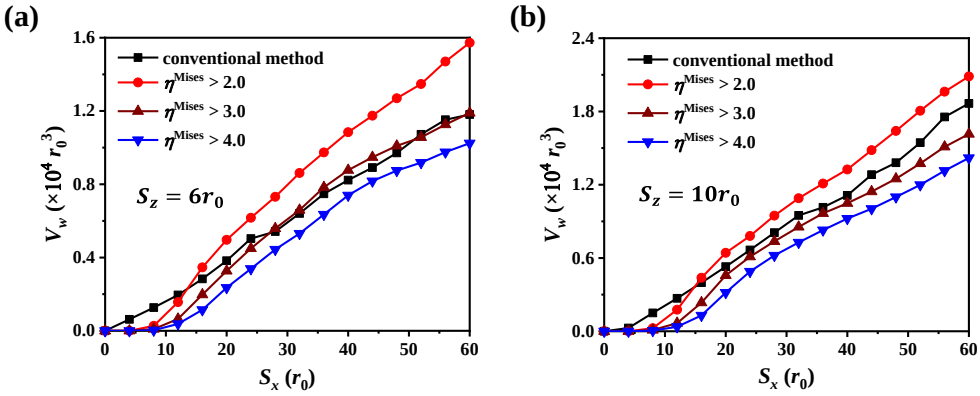

Fig. B2. Evaluation of the wear volume using different atomic equivalent strains as the threshold in material of $r_c = 1.38r_0$ when the scratching depths are (a) $S_z = 6r_0$ and (b) $S_z = 10r_0$.

Appendix C: Determination of plastic smoothing or fractured debris

For the asperity plowing, the asperity wear could originate from two different mechanisms,

i.e., the plasticity-induced asperity smoothing and the fractured wear debris. In the simulation, the formation of fractured wear debris is also accompanied by a large amount of plasticity. Therefore, it is crucial to have a criterion that determines which mechanism dominates the wear process. Here, a criterion is developed based on the formation of the new free surface: we first calculated the increase of the area of free surface ΔS by the analysis of construct surface mesh [47] when the plowing is finished, and then normalized the area ΔS by $2\pi R^2$ to calculate a dimensionless ratio η_f, i.e., $\eta_f = \Delta S/2\pi R^2$.

As shown in Fig. C1, good linearity can be observed between η_f and the normalized plowing depth α. For many data points that satisfy the observed linear relationship, we are sure that the wear mechanism is plasticity (from the deformed asperity topology); therefore, we believe that this linearity can be used as the criterion of plasticity dominated wear. For brittle asperity of radius larger than 30a, the η_f deviates from the linear relation due to the more significant increase of free surface generated by the asperity fracture. In this study, the plowing wear is considered to be fracture-dominated when $(\eta_f - \eta_0)/\eta_0 > 0.2$.

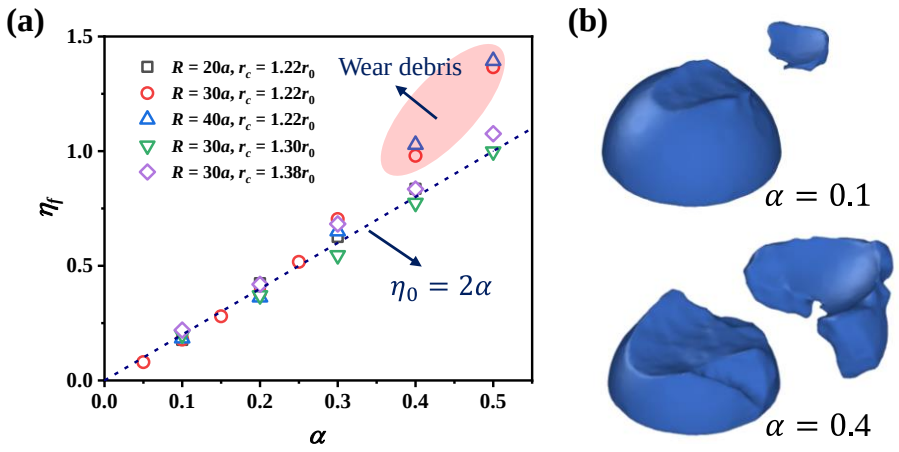

Fig. C1. (a) Increase of free surface in asperities due to plowing wear. (b) Illustration of two wear configurations in asperity with $r_c = 1.22r_0$ at different plowing depths, and the asperity radius is 30a.

Acknowledgement

This work was supported by the National Natural Science Foundation of China, Basic Science Center Program for "Multiscale Problems in Nonlinear Mechanics" (No.11988102), by

the National Natural Science Foundation of China (12172358, 11972347, 12022210, 12032001), and by Youth Innovation Promotion Association CAS (2018022).

CRediT authorship contribution statement

Jianqiao Hu: Conceptualization, Methodology, Investigation, Formal analysis, Writing-original draft. **Hengxu Song**: Conceptualization, Validation, Data curation, Project administration, Writing-review & editing. **Stefan Sandfeld**: Writing - review & editing, Funding acquisition. **Xiaoming Liu:** Project administration, Conceptualization, Writing-review & editing, Supervision, Funding acquisition. **Yueguang Wei**: Supervision, Resources.

Declaration of competing interest

The authors declare that they have no known competing financial interests or personal relationships that could have appeared to influence the work reported in this paper.

References

[1] K. Holmberg, A. Erdemir, Influence of tribology on global energy consumption, costs and emissions. Friction 2017; 5(3): 263-284.

[2] J.F. Archard, Contact and rubbing of flat surfaces. Journal of Applied Physics 1953; 24(8): 981-988.

[3] J.F. Archard, W. Hirst, The wear of metals under unlubricated conditions. Proceedings of the Royal Society of London. Series A. Mathematical and Physical Sciences 1997; 236(1206): 397-410.

[4] S.M. Hsu, M.C. Shen, A.W. Ruff, Wear prediction for metals. Tribology International 1997; 30(5): 377-383.

[5] M.Z. Huq, J.P. Celis, Expressing wear rate in sliding contacts based on dissipated energy. Wear 2002; 252(5-6): 375-383.

[6] J. Yan, A. Lindo, R. Schwaiger, A.M. Hodge, Sliding wear behavior of fully nanotwinned Cu alloys. Friction 2018; 7(3): 260-267.

[7] B. Bhushan, S. Sundararajan, Micro/nanoscale friction and wear mechanisms of thin films using atomic force and friction force microscopy. Acta Materialia 1998; 46(11): 3793-3804.

[8] K.-H. Chung, D.-E. Kim, Fundamental investigation of micro wear rate using an atomic force microscope. Tribology Letters 2003; 15(2): 135-144.

[9] R. Aghababaei, D.H. Warner, J.F. Molinari, Critical length scale controls adhesive wear mechanisms. Nature communications 2016; 7: 11816.

[10] K. Zhao, R. Aghababaei, Adhesive wear law at the single asperity level. Journal of the Mechanics and Physics of Solids 2020; 143: 104069.

[11] K. Zhao, R. Aghababaei, Interfacial plasticity controls material removal rate during adhesive sliding contact. Physical Review Materials 2020; 4(10): 103605.

[12] Y. Yang, L. Huang, Y. Shi, Adhesion suppresses atomic wear in single-asperity sliding. Wear 2016; 352-353: 31-41.

[13] Y. Yang, Y. Shi, Single asperity friction in the wear regime. Friction 2018; 6(3): 316-322.

[14] H. Song, H. Yavas, E.V.d. Giessen, S. Papanikolaou, Discrete dislocation dynamics simulations of nanoindentation with pre-stress: Hardness and statistics of abrupt plastic events. Journal of the Mechanics and Physics of Solids 2019; 123: 332-347.

[15] R. Aghababaei, K. Zhao, Micromechanics of material detachment during adhesive wear: a numerical assessment of Archard's wear model. Wear 2021; 476: 203739.

[16] S. Plimpton, Fast parallel algorithms for short-range molecular dynamics. Journal of Computational Physics 1995; 117(1): 1-19.

[17] A. Stukowski, K. Albe, Extracting dislocations and non-dislocation crystal defects from atomistic simulation data. Modelling and Simulation in Materials Science and Engineering 2010; 18(8): 085001.

[18] A. Stukowski, Visualization and analysis of atomistic simulation data with OVITO–the open visualization tool. Modelling and Simulation in Materials Science and Engineering 2010; 18(1): 015012.

[19] P. Zhu, R. Li, H. Gong, Molecular dynamics simulation of nanoscale abrasive wear of polycrystalline silicon. Crystals 2018; 8(12): 463.

[20] A. Li, I. Szlufarska, How grain size controls friction and wear in nanocrystalline metals. Physical Review B 2015; 92(7): 075418.

[21] F. Shimizu, S. Ogata, J. Li, Theory of shear banding in metallic glasses and molecular

dynamics calculations. Materials Transactions 2007; 48(11): 2923-2927.

[22] J. Hu, F. Yuan, X. Liu, Y. Wei, Effect of plasticity on nanoscale wear of third-body particles. Tribology International 2021; 155: 106739.

[23] J. Zhong, J.B. Adams, L.G. Hector, Molecular dynamics simulations of asperity shear in aluminum. Journal of Applied Physics 2003; 94(7): 4306-4314.

[24] J. Zhong, R. Shakiba, J.B. Adams, Molecular dynamics simulation of severe adhesive wear on a rough aluminum substrate. Journal of Physics D: Applied Physics 2013; 46(5): 055307.

[25] I. Hutchings, M. Gee, E. Santner, Friction and Wear. Springer Handbook of Materials Measurement Methods 2006: 685-710.

[26] H. Song, V.S. Deshpande, E. Van der Giessen, Discrete dislocation plasticity analysis of loading rate-dependent static friction. Proceedings of the Royal Society A: Mathematical, Physical and Engineering Sciences 2016; 472(2192): 20150877.

[27] R. Aghababaei, On the origins of third-body particle formation during adhesive wear. Wear 2019; 426-427: 1076-1081.

[28] Y. Mishin, M.J. Mehl, D.A. Papaconstantopoulos, A.F. Voter, J.D. Kress, Structural stability and lattice defects in copper:Ab initio, tight-binding, and embedded-atom calculations. Physical Review B 2001; 63(22): 224106.

[29] S. Foiles, M. Baskes, M. Daw, Embedded-atom-method functions for the FCC metals Cu, Ag, Au, Ni, Pd, Pt, and their alloys. Physical Review B 1986; 33(12): 7983-7991.

[30] F.H. Stillinger, T.A. Weber, Computer simulation of local order in condensed phases of silicon. Phys Rev B Condens Matter 1985; 31(8): 5262-5271.

[31] D. Kiener, A.M. Minor, Source-controlled yield and hardening of Cu(100) studied by in situ transmission electron microscopy. Acta Materialia 2011; 59(4): 1328-1337.

[32] Z. Wang, Z. Shan, J. Li, J. Sun, E. Ma, Pristine-to-pristine regime of plastic deformation in submicron-sized single crystal gold particles. Acta Materialia 2012; 60(3): 1368-1377.

[33] C.P. Frick, B.G. Clark, S. Orso, A.S. Schneider, E. Arzt, Size effect on strength and strain hardening of small-scale [111] nickel compression pillars. Materials Science and Engineering: A 2008; 489(1-2): 319-329.

[34] M.S. Colla, B. Wang, H. Idrissi, D. Schryvers, J.P. Raskin, T. Pardoen, High strength-

ductility of thin nanocrystalline palladium films with nanoscale twins: On-chip testing and grain aggregate model. Acta Materialia 2012; 60(4): 1795-1806.

[35] K.N. Jonnalagadda, I. Chasiotis, S. Yagnamurthy, J. Lambros, J. Pulskamp, R. Polcawich, M. Dubey, Experimental Investigation of Strain Rate Dependence of Nanocrystalline Pt Films. Experimental Mechanics 2009; 50(1): 25-35.

[36] M. Chen, L. Petho, A.S. Sologubenko, H. Ma, J. Michler, R. Spolenak, J.M. Wheeler, Achieving micron-scale plasticity and theoretical strength in Silicon. Nature communications 2020; 11(1): 2681.

[37] A. Chauniyal, G. Dehm, R. Janisch, On the role of pre-existing defects in influencing hardness in nanoscale indentations — Insights from atomistic simulations. Journal of the Mechanics and Physics of Solids 2021; 154: 104511.

[38] J. Hu, X. Ye, X. Liu, Z. Chen, The effects of initial void and dislocation on the onset of plasticity in copper single crystals. Journal of Applied Physics 2019; 126(16): 165104.

[39] R.-G. Xu, H. Song, Y. Leng, S. Papanikolaou, A molecular dynamics simulations study of the influence of prestrain on the pop-In behavior and indentation size effect in Cu single crystals. Materials 2021; 14(18): 5220.

[40] M. Mishra, I. Szlufarska, Dislocation controlled wear in single crystal silicon carbide. Journal of Materials Science 2012; 48(4): 1593-1603.

[41] J. Sun, L. Fang, J. Han, Y. Han, H. Chen, K. Sun, Abrasive wear of nanoscale single crystal silicon. Wear 2013; 307(1-2): 119-126.

[42] J. Hu, H. Song, Z. Liu, Z. Zhuang, X. Liu, S. Sandfeld, Predicting the flow stress and dominant yielding mechanisms: analytical models based on discrete dislocation plasticity. Scientific reports 2019; 9(1): 20422.

[43] S. Papanikolaou, H. Song, E. Van der Giessen, Obstacles and sources in dislocation dynamics: Strengthening and statistics of abrupt plastic events in nanopillar compression. Journal of the Mechanics and Physics of Solids 2017; 102: 17-29.

[44] H. Song, R.J. Dikken, L. Nicola, V.D.E. Giessen, Plastic ploughing of a sinusoidal asperity on a rough surface. Journal of Applied Mechanics 2015; 82(7): 071006.

[45] H. Song, S. Papanikolaou, From statistical correlations to stochasticity and size effects in

sub-micron crystal plasticity. Metals 2019; 9(8): 835.

[46] P. Zhu, Y. Hu, T. Ma, H. Wang, Study of AFM-based nanometric cutting process using molecular dynamics. Applied Surface Science 2010; 256(23): 7160-7165.

[47] A. Stukowski, Computational analysis methods in atomistic modeling of crystals. JOM 2013; 66(3): 399-407.

Breakdown of Archard law due to transition of wear mechanism from plasticity to fracture

Jianqiao Hu [a,b], Hengxu Song [c*], Stefan Sandfeld [c,d], Xiaoming Liu [a,b*], Yueguang Wei [e]

[a] State Key Laboratory of Nonlinear Mechanics, Institute of Mechanics, Chinese Academy of Sciences, Beijing 100190, P R China

[b] School of Engineering Science, University of Chinese Academy of Sciences, Beijing 100049, P R China

[c] Institute for Advanced Simulation, IAS-9: Materials Data Science and Informatics, Forschungszentrum Juelich GmbH, Juelich 52425, Germany

[d] Faculty 5, RWTH Aachen University, 52062 Aachen, Germany

[e] Department of Mechanics and Engineering Science, College of Engineering, Peking University, Beijing 100871, P R China

[*]*Corresponding authors:* *H.Song@fz-juelich.de, xiaomingliu@imech.ac.cn*

Abstract:

Widely used to quantify material wear, the Archard wear law was derived from the asperity flattening model. However, the flattening model is so idealized that it cannot properly represent the real situation with general interlocked asperities, where asperity plowing dominates the wear instead of shearing flattened asperity. Using molecular dynamics simulations, we discussed if Archard law can hold during plowing wear of interlocked interface. Our results indicated Archard law breaks down when fracture dominates the wear. Furthermore, increasing interfacial adhesion or decreasing material ductility changes the dominant wear factor from plasticity to fracture. Finally, we proposed a criterion to determine when Archard wear law will break down and discussed the proposed criterion for real materials.

Keywords:

Archard wear law; Molecular dynamics; Asperity plowing; Dislocation plasticity; Fractured debris.

Nomenclature

a	lattice constant of FCC crystal
a_c	contact radius during flattening
d^*	critical junction size
F_z	normal force between asperities
G	shear modulus
H	material hardness
h	plowing depth
K_w	wear coefficient
k_0	specific wear rate
l_a	junction size of asperity plowing
l_x, l_y, l_z	substrate size
P	normal load between contact surfaces
R	radius of hemispherical asperity
r_c	cut-off radius for coarse-grained potentials
r_0	unit length for coarse-grained potentials
R_c, R_{MD}, R_{Exp}	critical asperity radius
t_0	unit of time
V_w	wear volume
V_a	volume of hemispherical asperity
α	normalized plowing depth, h/R
$\sigma_j, \sigma_{MD}, \sigma_{Exp}$	shear strength
η^{Mises}	atomic equivalent strain
Δw	surface energy
λ	adhesion ratio
λ_s	shape factor
ρ_{ini}	initial dislocation density
η_0, η_f	normalized area of new surface

1. Introduction

Material wear between surfaces in contact during relative sliding widely exists in modern industry. It was reported that 3% of the global energy consumption is used to remanufacture worn parts and spare equipment due to wear and wear-related failures [1]. Despite the importance of wear on energy saving and economic growth, our understanding of wear unfortunately still hovers around the famous Archard wear law which was proposed in 1953. According to the Archard law [2], the volume of the worn material dV is proportional to the normal load P and the sliding distance ds, and inversely proportional to the material hardness H: $dV = K_w Pds/H$ with K_w being the wear coefficient. The interpretation of the Archard wear law is based on the hypothesis of energy dissipation: Pds is proportional to the external work done by the friction force, and the dissipation through the plastic deformation is represented by H. A severe plastic deformation results in material wear.

The derivation of the Archard wear law is straightforward based on the flattened asperity model, as shown in Fig. 1(a). The asperity is plastically flattened by a normal load F_z, resulting in a contact radius of a_c. The normal load F_z can be calculated as $F_z = \pi a_c^2 H$. It is further assumed with the sliding distance $ds = 2a_c$, that the generated wear volume is proportional to the volume of a hemisphere of radius a_c: $dV = \gamma \frac{2}{3}\pi a_c^3$ where γ is a proportionality parameter. Therefore, the wear volume per unit sliding distance can be calculated as

$$\frac{dV}{ds} = \frac{\gamma \frac{2}{3}\pi a_c^3}{2a_c} = \frac{\gamma}{3}\pi a_c^2 = \frac{\gamma}{3}\frac{F_z}{H} = K_w \frac{F_z}{H}, \tag{1}$$

where K_w is known as the wear coefficient.

On the rough surface level, the total wear volume is the summation of the material wear at all asperities. Therefore for the macroscopic surface, the wear volume can be calculated by:

$$\frac{dV}{ds} = K_w \frac{\sum F_z}{H} = K_w \frac{P}{H}. \tag{2}$$

Here P is the total normal load on the surface.

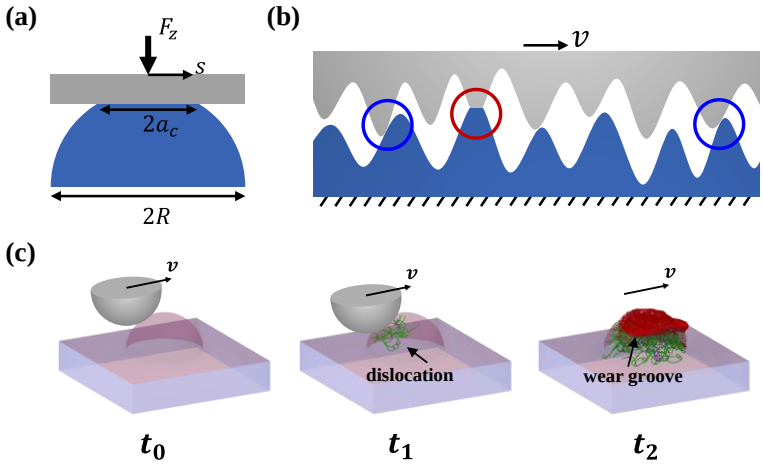

Fig. 1. (a) 2D schematic of the wear process based on the 3D flattened asperity model. The asperity is compressed by a normal load F_z and then sheared by a displacement of *s*. (b) Schematic of asperity configurations during the relative sliding between rough surfaces. Red circle highlights the flattened asperities, and blue circles highlight the plowing asperities. (c) Asperity configuration at different times during the asperity plowing process. Dislocations are shown at the time of t_1 and t_2; the red atoms at t_2 (the upper asperity is not shown) are worn atoms.

Although the Archard wear law has been widely used to quantify the material wear in tribological experiments [3-6], the direct confirmation of the flattened asperity model was not possible until the extensive studies of wear characteristics of atomic force microscopy tips, where the asperity fracture happens at certain circumstances [7, 8]. Recently, it has been shown through molecular dynamics (MD) simulations [9] that there exists a critical length scale that controls the formation of wear debris at the asperity level:

$$d^* = \lambda_s \cdot \frac{\Delta w}{(\sigma_j^2/G)}, \tag{3}$$

where G is the shear modulus and σ_j is the shear strength of the junction (the weaker one of the bulk material shear strength and the adhesion strength), Δw is the energy associated to newly created free surfaces, and λ_s is a shape factor. Junctions with size larger than d^* produce the fracture-induced debris while the smaller ones deform plastically. Recent MD studies by Zhao and Aghababaei [10, 11] simulated the wear between an asperity and a rigid platen (similar to the schematic in Fig. 1(a)); the simulation results confirmed the Reye wear law (the wear volume is linearly proportional to the work of frictional load) holds only when

the plastic deformation of the asperity dominates the wear. By performing a rigid flat tip sliding over a single asperity, Yang et al. [12, 13] studied material wear under different normal contact stresses: when the contact stress is small, material wear is caused by interfacial adhesion via atom-by-atom attrition; when the contact stress is large, material wear is caused by the plastic flow. In the above models, the role of adhesion seems to be overestimated because of their model setup: adhesion is necessary to transfer the shear loading; without adhesion, there will be essentially no wear in their models. In addition, these analyses based on the flattened asperity model cannot explain why the Archard wear law is commonly observed during the wear of real rough surfaces, as shown in Fig. 1(b). There, instead of the flattened asperity in the red circle, interlocking asperities in blue circles are more commonly seen. Therefore, it is crucial to confirm whether the Archard wear law still holds for the case of asperity plowing. Furthermore, most of the above numerical studies are carried out based on pristine crystals, while the initial defects greatly affect the plastic deformation at small scales [14]. Then, another issue arises how the initial defects affect asperity plowing and thus the Archard wear law.

In this paper, through MD simulations shown in Fig. 1(c), we try to address the question: Is the Archard wear law still satisfied for asperity plowing over a wide range of plowing conditions, including asperity size, plowing depth, and material ductility? First, using a series of model materials, we clarified when and how the Archard law breaks down in the plowing wear. Based on all case studies, we proposed a criterion for the transition of the wear mechanism. Then, the critical size for the transition is discussed in pristine crystals and crystals with initial defects for the model materials. In addition, the extension of our model is carried out for some real materials. Taking copper as an example, we clarified the role of adhesion on the material wear, which was not properly addressed in the flattened asperity models published previously [10, 11, 15]. The paper is organized as follows: Section 2 presents the MD modeling details and the definition of material wear at the atomic scale. In Section 3, we study the plowing wear and determine the wear condition for the breakdown of Archard law. The effect of initial dislocations on wear is also discussed. Section 4 further explores the plowing wear for several common materials, with the contact interface being both non-adhesive and adhesive. Finally, Section 5 summarizes our findings.

2. Model description and methodology

To understand the wear law for different materials at the asperity level, we performed MD simulations of the asperity plowing with a group of virtual materials characterized by coarse-grained potentials developed recently [9]. Compared to the conventional potentials used in the MD simulations, the modified coarse-grained potential (see Appendix A) has the advantage that the material's brittle/ductile property can be tuned without changing the elastic properties. This provides an opportunity to study the effect of material ductility on the wear process. In this study, all MD simulations are carried out by employing the Large-scale Atomic/Molecular Massively Parallel Simulator [16]. In this section, we first describe the model setup of asperity plowing and then introduce the definition of wear.

2.1 The model setup of asperity plowing

The plowing model contains two hemispherical asperities and a substrate, as shown in Fig. 2. The two asperities have the same radius of R, and the lower asperity is located at the center of the substrate. The lengths of the substrate in the x and y directions are the same (i.e., $l_x = l_y$), and the thickness in z direction is l_z. The dimensions of the substrate are listed in Table 1 for materials with coarse-grained potentials.

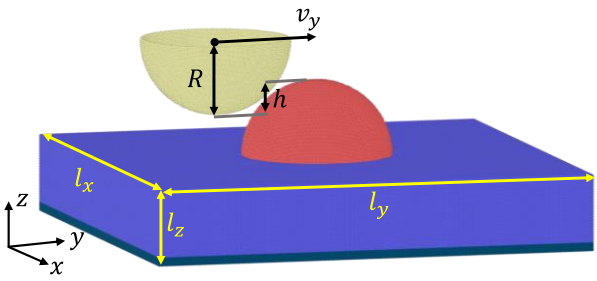

Fig. 2. Geometrical model of the asperity plowing.

For all simulations, the asperity and the substrate are all assumed with a face-centered cubic (FCC) structure. The upper hemispherical asperity is set to rigid, and the lower asperity and the substrate are deformable with the same material. The x, y, and z-axes of the lower asperity and the substrate are oriented in the [100], [010], and [001] lattice directions, respectively. Periodic boundary conditions are employed along the x and y directions, and the free boundary condition is adopted along the z direction. At the bottom of the substrate, atoms

with a thickness of $0.1R$ are fixed; other atoms in the lower asperity and substrate obey the classical Newton's second law. For all simulations, we defined the normalized plowing depth as $\alpha = h/R$. In the analysis, we used the dislocation extraction algorithm (DXA) [17] to track dislocations, and used the open-source software OVITO [18] to visualize the defects.

2.2 Simulation Parameters with modified potentials

Prior to the plowing, the model is first relaxed at a temperature of $0.005\varepsilon/k_B$ for $50t_0$ (k_B is the Boltzmann constant, and t_0 is the reduced time unit) to achieve the minimum energy. Then, at the plowing depth α, the upper rigid asperity moves along *y* direction at a constant velocity of $0.1a/t_0$. During the plowing, the temperature is enforced to $0.005\varepsilon/k_B$ using the Nose´-Hoover thermostat. In addition, the simulations of asperity wear were also performed at a lower plowing velocity ($0.05a/t_0$) and a higher temperature of $0.05\varepsilon/k_B$, and this alters the results only negligibly (see Supplementary Material). The parameters are summarized in Table 1.

Table 1 Parameters for asperity plowing with coarse-grained potentials.

Parameters	Values/expression
Deformable asperity radius	R = 30a, a (lattice constant)= $\sqrt{2}r_0$
Rigid asperity radius	R = 30a
Substrate size	l_x = 6R, l_y = 6R, l_z = R
Time step (t_0)	0.0025
Temperature (ε/k_B)	0.005
Plowing velocity (a/t_0)	0.1
Plowing depth (α)	0.1~0.6
Plowing direction	[010] on (001) surface

Using the plowing model with coarse-grained potentials, we studied the asperity wear in materials of different ductile properties. The effect of interfacial adhesion can be checked by changing the cohesion energy with an adhesion factor λ where a larger value of λ denotes

stronger interfacial adhesion. The potential used between the asperity pairs, if not explicitly stated, is the same as the one used within the lower asperity, indicating the interfacial strength between asperities is the same as the strength of the bulk asperity.

2.3 Definition of wear in asperity plowing

The conventional criterion to determine the "worn atoms" is based on a certain threshold of atomic position or velocity. For example, in the MD simulations of nano scratching on an atomistic flat surface, the worn atoms are evaluated as the atoms located above the original substrate surface [19] (which we term as the conventional wear criterion) or the atoms with velocities approaching the sliding velocity of the tip [20]. However, these methods cannot be used to define the worn atoms for asperity plowing due to the complex geometries and the large deformations. We utilize the atomic equivalent strain η^{Mises} [21] to define the worn atoms. The critical η^{Mises} is calibrated in the following way [22]: for given materials, we carried out nano-scratching simulations on a flat surface. The wear volume, which is calculated by multiplying the number of worn atoms and the volume of a single atom in a perfect crystal, is firstly evaluated by the conventional wear criterion, then the wear volume is evaluated again using the atomic equivalent strain criterion to determine the critical η^{Mises}.

For example, for copper, we calibrated the critical η^{Mises} to be 1.5. The critical η^{Mises} is not a universal value, therefore, for new 'materials', this calibration needs to be repeated. The details of the calibration can be found in Appendix B. For cases with coarse-grained potentials, we utilized the same method to determine the threshold strain for worn atoms. The result showed that the threshold strain is different when the material's ductility varies (details can be found in Appendix B). Furthermore, we found that the atomic strain criterion can describe the worn atoms only when plasticity dominates the asperity wear and it becomes invalid for fracture-induced wear debris. Because of this limitation, we combined the wear criterion that has been used in the adhesive plowing model [23, 24]: the atoms removed from the lower asperity are also considered as worn atoms. As a result, the atoms with atomic equivalent strain larger than the critical η^{Mises} and the atoms removed from the lower asperity are considered as worn atoms in our simulations.

3. Breakdown of Archard law due to asperity fracture

In order to see whether the Archard wear law holds for different materials, we utilized the coarse-grained interatomic potentials developed by Aghababaei et al. [9] to perform the plowing simulations. Details of the interatomic potentials can be found in Appendix A. Basically, the cut-off radius r_c in Eq. (9) controls the material ductility. The case with $r_c = 1.22r_0$ characterizes a brittle material while another case with $r_c = 1.38r_0$ describes a ductile material.

3.1 Plowing wear of single asperity

In a scratch of single asperity, the increase of the normal load would lead to a larger plowing depth. Here, we first quantified the wear for different plowing depths during the adhesive plowing in materials of $r_c = 1.22r_0$. Fig. 3(a) shows the evolution of the wear volume with the increasing plowing distance at different plowing depths. For one plowing depth, the wear volume initially increases with the increasing plowing distance, then saturates. We take the wear volume when the plowing is finished as the final wear volume. When the plowing depth exceeds 0.4, the final wear volume does not always increase. This is due to the transition of the wear mechanism from plasticity to fracture when the plowing depth is larger than ~0.4. To determine whether the plowing wear is dominated by plasticity smoothing or fractured wear debris, we developed a criterion based on the formation of free surface to identify the wear mechanism (see Appendix C).

Fig. 3(b) illustrates the atomic strain with two plowing depths at the end of plowing. For the plowing depth of $\alpha = 0.1$, the asperity tip is chopped and flattened, i.e., asperity smoothing takes place. In this situation, only a few worn atoms are generated. Correspondingly, very few dislocations are left in the asperity, as shown in Fig. 3(c). By analyzing the dislocation structures during plowing, we confirmed that dislocations initially nucleate at the contact region; however, the nucleated dislocations finally annihilate at the free surface of asperity due to image forces. In contrast, for the large plowing depth of $\alpha = 0.5$, the asperity is fractured to form irregular debris. At the same time, numerous dislocations are generated during plowing (see Fig. 3(c)). The asperity deformation associated with these dislocation activities can be seen in Fig. 3(b),

where atomic strain larger than the defined strain criterion ($\eta^{\mathrm{Mises}} \geq 6.0$) can be found with a large volume. Also, we noticed that some atoms removed from the lower asperity have atomic strain less than the critical value. However, these atoms are also considered as worn atoms and contribute to the wear volume in Fig. 3(a).

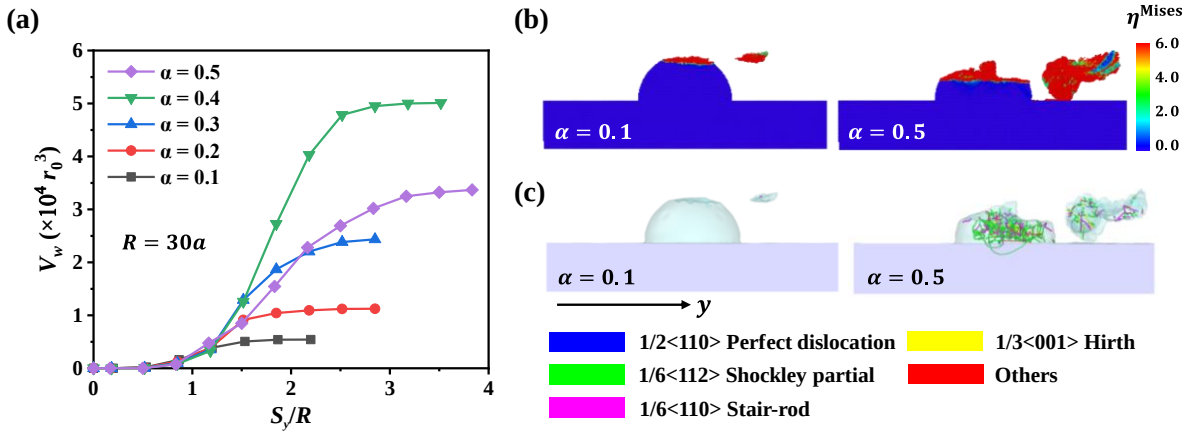

Fig. 3. (a) Evolution of wear volume with increasing plowing distance in asperity with radius of 30a. (b) Distribution of atomic equivalent strain and (c) dislocation structures at the time when the plowing is finished. The upper rigid asperity is not shown.

3.2 Breakdown of Archard law in brittle asperity

In our simulation, we can rewrite the Archard wear law as

$$V_w = \int dV = K_w v_y \int F_z/H \cdot dt. \quad (4)$$

Here, V_w and v_y are the wear volume and the sliding velocity, respectively. We introduced a parameter E_z to consider the combined effect of the normal load and the plowing distance at the asperity level, $E_z = v_y \int F_z \cdot dt$. By flattening asperities of different sizes, we found that the flatten hardness H is almost size independent for asperity with radius ranging from 20a to 40a (see Supplementary Material); therefore, we can further rewrite Eq.(4) as

$$V_w = k_0 E_z. \quad (5)$$

Here, $k_0 = K_w/H$ is the so-called specific wear rate [25].

By analyzing the plowing wear in materials of different ductility, we found that Archard law holds for ductile material but breaks for brittle material. Fig. 4(a) summarized the results of adhesive plowing for materials of different ductility in terms of Eq. (5). For the ductile materials ($r_c = 1.30r_0$ and $r_c = 1.38r_0$), good linearity can be observed for asperity wear and

k_0 is roughly a constant. Therefore, the Archard wear law remains valid. Correspondingly, the dominant wear mechanism for ductile asperities at the plowing depth of 0.5 is plastic smoothing rather than fractured wear debris, as shown in Fig. 4(b). In contrast, for the brittle material ($r_c = 1.22r_0$), the Archard law is satisfied only at a smaller value of E_z which corresponds to the shallow plowing depth. However, for brittle asperity at the plowing depth of 0.5 (see Fig. 3), the fracture-induced wear debris forms, thus breaking the Archard wear law.

In addition to the material ductility, interfacial adhesion may also play a vital role in the validity of Archard law. As shown in Fig. 4(a), when the adhesion strength is reduced to $\lambda = 0.6$, the Archard wear law is recovered even at the larger plowing depth. The corresponding wear morphology (last row of Fig. 4(b)) becomes asperity smoothing, i.e., for weak adhesion, the fracture-induced debris won't form. We also studied the non-adhesive plowing for materials of different ductility; it is concluded that Archard law always holds because the dominant wear mechanism is plasticity which is exactly the fundamental assumption of Archard law.

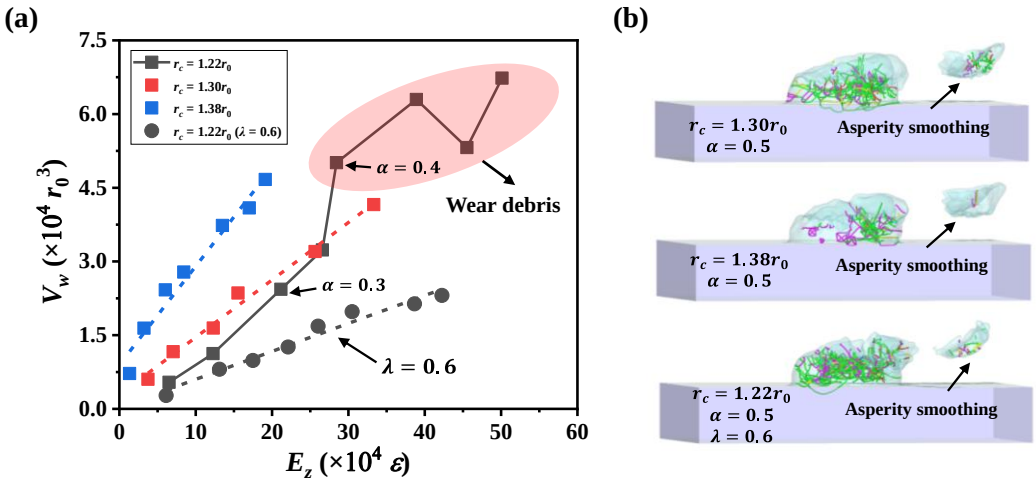

Fig. 4. (a) Wear volume as the function of E_z in asperity of radius 30a. (b) Dislocation structures in asperity with different plowing conditions.

3.3 A model to determine the breakdown of Archard law

From the above results and analysis, we can conclude that the failure of the Archard wear law is attributed to the transition of the wear mechanism from the plasticity-induced asperity smoothing to the fracture-induced wear debris. The question of when this transition happens for a given asperity remains elusive. For plowing asperities, the question essentially includes

two aspects: how large the asperity has to be, and how deep the plowing depth should be to generate the fracture-induced debris to fail the Archard wear law.

In the plowing model of a hemisphere of radius R and plowing depth α, the junction size during the plowing process can be estimated as $l_a = \sqrt{4\alpha - \alpha^2}R$ based on geometric analysis. Particularly, $l_a^{max} = \sqrt{3}R$ by assuming the maximum depth $\alpha = 1.0$. From Eq. (3), the minimum junction size to form fracture is $d^* = \lambda_s \cdot \frac{\Delta w}{(\sigma_j^2/G)}$. By combining l_a and d^*, the plowing depth α to form fracture can be derived as $2 - \sqrt{4 - \left(\frac{d^*}{R}\right)^2}$.

Furthermore, we proposed a critical asperity size by combining the expressions of l_a^{max} and d^*, and the critical size can be expressed by:

$$R_c = \frac{\lambda_s}{\sqrt{3}} \cdot \frac{\Delta w}{(\sigma_j^2/G)}. \quad (6)$$

When the asperity size R is smaller than R_c, the Archard wear law always holds. This is because the wear is controlled by plastic deformation independent of the plowing depths. When the asperity size R is larger than R_c, the Archard wear law will hold only when the plowing depth satisfies $\alpha < 2 - \sqrt{4 - \left(\frac{d^*}{R}\right)^2}$. In Eq.(6), σ_j is the smaller value between the interfacial strength and the asperity yield strength (or the apparent yield strength due to the combination of decohesion and plasticity, as discussed in [26]), this fact indicates that R_c will be a large value for non-adhesive plowing (σ_j is very small for non-adhesive case). Note that this critical size is proposed based on the assumption that the two asperities have the same radius. For two plowing asperities with different radii, the geometric analysis would yield a different result, but the fundamental findings still hold that the Archard wear law breaks down due to the formation of fractured wear debris.

Based on the above analysis, we now reinterpret our simulation results. For the brittle material with $r_c = 1.22r_0$, the critical junction size d^* is $43 \pm 9r_0$ based on the shear strength determined by flattening (see Supplementary Material), which is consistent with $50r_0$ in [27]. For the critical junction size of $50r_0$, the corresponding critical radius R_c is around $29r_0$ from Eq.(6). When the asperity size R is $30a$ with $a = \sqrt{2}r_0$, the critical plowing depth $\alpha = \sim 0.38$. Our simulation results (see Fig. 4(a)) are consistent with this analytical prediction that the wear mechanism is the asperity smoothing when the plowing depth is 0.3, and becomes

fracture-induced debris as the depth increases to 0.4.

Fig. 5 further confirms the breakdown of the linear wear law due to the wear mechanism changing to fracture-dominated. Fig. 5(a) shows the wear volume as a function of E_z for asperity with the radius of $20a$ over a wide range of plowing depths α from 0.1 to 0.5; the linearity shows clear Archard law, and microstructure analysis indicates a consistent finding of the plasticity-induced asperity smoothing. Because the asperity size is less than R_c (~$29r_0$) from Eq.(6), the asperity wear is dominated by plasticity, so the Archard wear law remains valid. While in another example of Fig. 5(b), for asperity with the radius of $40a$ (larger than R_c), the transition of wear mechanism occurs as the plowing depth increases to 0.4. With plowing depth α larger than 0.4, the Archard wear law breaks down.

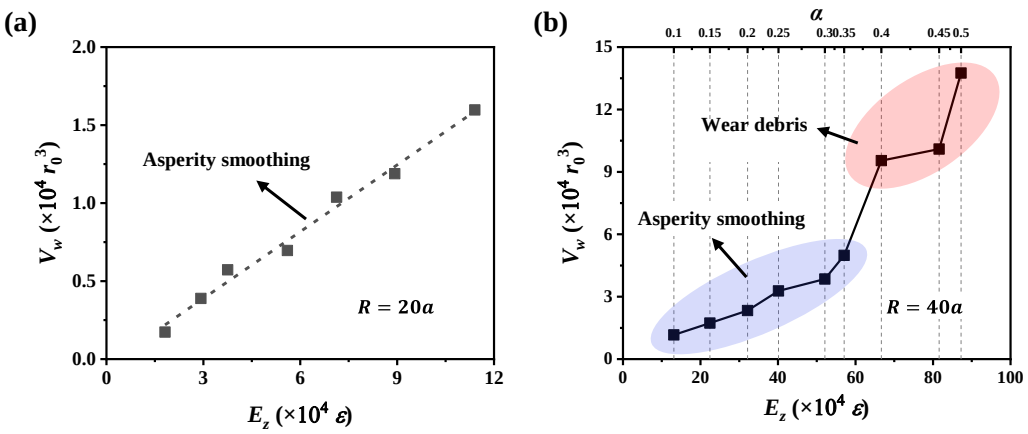

Fig. 5. Wear volume as a function of E_z in asperity with (a) $R = 20a$, and (b) $R = 40a$ in material of $r_c = 1.22r_0$. The plowing depths are also shown for asperity with radius of $40a$.

Furthermore, the effect of the reduced adhesion in Fig. 4 can be well understood: when the interfacial adhesion is reduced by $\lambda = 0.6$, R_c is calculated to be ~$80r_0$ from Eq.(6), while the asperity size is $30\sqrt{2}r_0$ in the simulations. Therefore, asperity wear is dominated by plasticity, and the Archard wear law still holds. For $r_c = 1.30r_0$ and $r_c = 1.38r_0$, R_c is ~$59r_0$ and ~$113r_0$ respectively; therefore, if the asperity size $30\sqrt{2}r_0$ less than R_c is used in our simulations, the Archard wear law should always hold.

3.4 Increased critical size due to initial dislocations

The above analysis for plowing wear is all based on pristine asperity with no initial defects. However, for actual materials, initial defects widely exist. In this section, we further studied the

plowing wear in asperities with initial defects.

The initial defects in the asperity are prepared by the following. The pristine asperity is first stretched along the *x* and *y* directions to a certain strain and then released to the state with no external load. By applying different strain magnitudes, we can get asperities with dislocations of different densities, as shown in Fig. 6(a). It was found that the wear mechanism tends to become the plasticity-induced asperity smoothing with increasing initial dislocation density. As shown in Fig. 6(b), for brittle asperity with a low dislocation density of $0.002r_0^{-2}$, the debris embryo forms due to the formation of crack. However, these cracks do not propagate and combine to form individual debris, so the plowing wear is still considered to be dominated by plasticity. In contrast, for asperity with initial dislocation density higher than $0.008r_0^{-2}$, the deformation becomes smoother without crack formation during plowing.

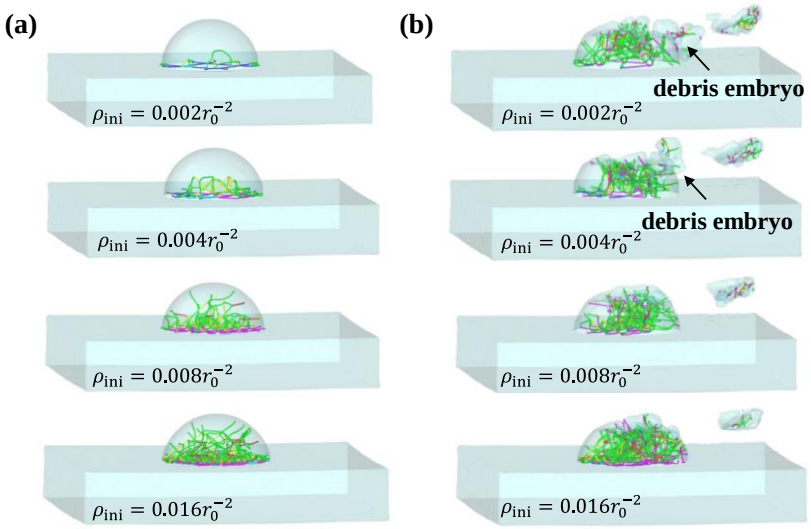

Fig. 6. Transition of wear mechanism in brittle asperity ($r_c = 1.22r_0$) with initial dislocations. (a) Initial dislocations in asperities, and (b) dislocation structures at the time when the plowing is finished. The plowing depth is 0.4.

Due to the existence of initial dislocations, the material becomes more ductile and thus leads to a larger critical size for the transition of wear mechanism. For asperity with initial dislocations, we first determined the shear strength by flattening the asperity (see Supplementary Material) and then obtained the critical size based on the analytical model in section 3.3. The simulation results are consistent with the analytical model that the dominant wear mechanism changes to the fractured wear debris when the plowing depth exceeds ~0.5, as

shown in Fig. 7.

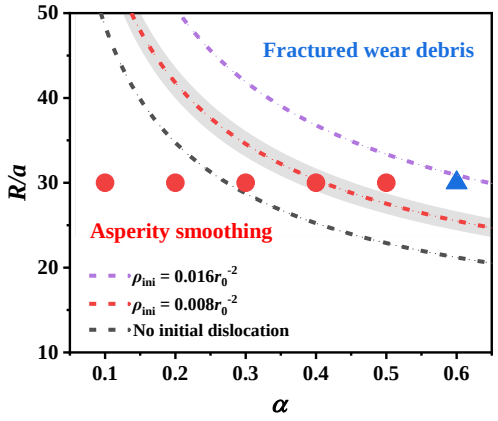

Fig. 7. The transition of wear mechanism due to the existence of initial dislocations. The dash lines are obtained by the analytical model, and the red dots are simulation results for asperity with $\rho_{ini} = 0.008r_0^{-2}$. The red shaded region for the case of $\rho_{ini} = 0.008r_0^{-2}$ corresponds to the variation of shear strength.

4. Archard wear law for real materials

From the above analysis, it can be seen that the Archard wear law breaks down as the wear mechanism changes from plasticity-induced asperity smoothing to fractured wear debris. In this section, the critical size for the transition of wear mechanism is further discussed for some real materials. Taking copper as an example, we carried out MD simulations for plowing copper asperity with EAM potential to check the Archard wear law. What is more, the non-adhesion plowing is discussed as a special case for copper asperity.

4.1 Critical size for the transition of wear mechanism

Using Eq. (6), we can roughly estimate the critical asperity size R_c below which the plasticity dominates the asperity wear. As shown in Table 2, we estimated six materials of different ductility and calculated their critical size for the transition of the wear mechanism. The material properties, including the surface energy and the shear modulus, are obtained from the literature of the potential function [28-30]. In the estimation, the surface energy is calculated on the (100) surface for Si with the diamond crystal (DC) structure, and the experimental average surface energy [29] was used for the FCC crystals. We used C_{44} in the fourth-order

elastic moduli as the shear modulus. The critical asperity radius for the wear transition in each material was discussed based on two sets of shear strength. First, for pristine crystals, i.e., no initial defects exist, the shear strength σ_{MD} is obtained through $\sigma_{MD} = \frac{1}{3\sqrt{3}}H$, where H is the material hardness determined by the indentation simulation using the similar way in Appendix A. All the indentations are performed on the (001) surface with a temperature of 300 K and an indentation velocity of 10 m/s. Second, the shear strength σ_{exp} for each material is also taken from their experimental measurements of open literature [31-36]. The two sets of shear strength differ greatly, on the one hand, because the indentation simulation starts with a pristine crystal, while for materials with initial defects [14, 37, 38], the yield stress is much lower; on the other hand, the indenter size used in MD is usually very small, and the calculated hardness has strong indentation size effect [39]. Based on the above two sets of shear strength, we can calculate the corresponding critical asperity radius, i.e., R_{MD} and R_{Exp} in Table 2. These two critical radii are also compared in Fig. 8.

Table 2 Predicting the critical asperity size for six typical materials.

Material	Cu	Au	Ni	Pd	Pt	Si
Lattice constant (Å)	3.615	4.08	3.52	3.89	3.92	5.431
Shear modulus (GPa)	76.2	45	128	65	68	56.4
Surface energy (mJ/m^2)	1790	1500	2380	2000	2490	2356
Crystal structure	FCC	FCC	FCC	FCC	FCC	DC
Shear strength, σ_{MD} (GPa)	1.622	0.913	2.428	1.245	1.329	2.209
Critical asperity radius, R_{MD} (nm)	179.6	280.5	179.0	290.5	332.1	94.5
Shear strength, σ_{Exp} (GPa)	0.1~0.5	0.13~0.25	0.1~0.6	0.25~0.6	~0.65	2.0~4.0
Critical asperity radius, R_{Exp} (10^3 nm)	1.9~47.2	3.7~13.8	2.9~105.5	1.3~7.2	~1.4	0.03~0.12

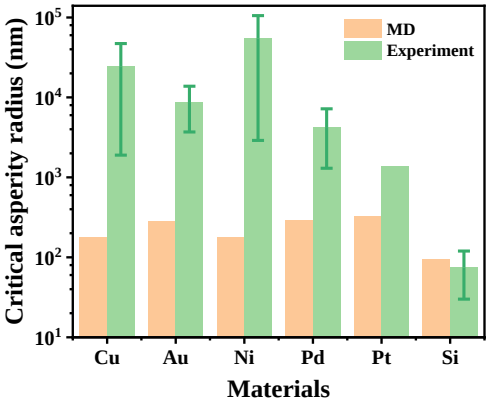

Fig. 8. The critical asperity size for the transition of wear mechanism in six typical materials. The experimental predictions are calculated based on the strength of Cu [31], Au [32], Ni [33], Pd [34], Pt [35], and Si [36].

From Table 2 and Fig. 8, it can be seen for pristine crystals, the critical asperity size R_{MD} is around a hundred nanometers for Si and a few hundred nanometers for other ductile metals. Experimentally, in the wear of Si atomic force microscopy (AFM) probes, the formation of wear debris was observed as the asperity size is larger than 100 nm [8]. However, these length scales are beyond the dimensions that MD simulations can handle; therefore, even for brittle materials such as Si, the plastic deformation rather than the formation of the fractured debris was widely observed in MD simulations of the wear process [40, 41].

The simple estimation based on the pristine crystals matches the wear process at a very small scale (below 100 nanometers) where materials could be assumed to be pristine. However, at the larger length scale, initial defects in the material, here we only consider initial dislocation microstructures, have a great influence on the material strength, therefore 'redefine' the critical asperity size. This is more likely to be the case in the real material, thus we estimated the critical asperity size based on the experimentally measured material strength. It can be seen from Fig. 8 that the critical asperity size R_{Exp} for ductile materials ranges from several micron meters to hundred micron meters. These length scales essentially imply that plastic deformation dominates the wear process in the rough surface, i.e., Archard wear law holds, because the fractured debris forms in asperity of the size of micron meters which is normally larger than the roughness of the material, i.e., there won't be a perfect asperity of this size on the rough surface.

In contrast, for Si, with the initial defects considered, the critical length scale can be even smaller than the estimation of its pristine counterpart, i.e., fractured debris may be in fact even easier to form.

The above discussion highlights the fact that even though Eq. (6) gives an estimation of the critical asperity size, the material strength involved in the estimation is much more complex than it seems. Any direct application/extension of Eq. (6) to the rough surface wear should be taken with special care. The initial dislocation microstructures [42, 43], the surface topology [44], and the material deformation history [45] all have a huge influence on the material yield strength.

4.2 Discussion on plowing wear of copper as an example

From the above discussion on critical size in real materials, we can expect that for the plowing wear of copper in MD simulations, the Archard wear law always holds because of the size constraints for MD simulations. In this section, as an example, we revisited the validity of the Archard wear law in copper asperity with both non-adhesive and adhesive plowing.

4.2.1 Parameters for plowing of copper asperity

Similar to the plowing of asperity with modified Morse potentials, the copper model with more real potential (EAM) is relaxed at a temperature of 0.01 K for a time span of 150 ps (in total 10^5 time steps) to achieve the minimum energy. Subsequently, the upper rigid asperity moves along the *y* direction at a constant velocity of 36 m/s (which corresponds to 0.1*a*/ps with *a* being the lattice constant). During plowing, the Nose´-Hoover thermostat was adopted to keep the active atoms at the temperature of 0.01 K. To study the size effect, the radius of the copper asperity varies from 5*a* to 50*a* where *a* is the lattice constant. The above parameters are also summarized in Table 3.

Table 3 Parameters used in the plowing of copper asperity.

Parameters	Values/expression
Deformable asperity radius	R = 5a~50a; a (lattice constant) = 3.615 Å

Rigid asperity radius	The same as the deformable asperity
Substrate size (repulsive potential)	l_x = 4R, l_y = 4R, l_z = 0.8R
Substrate size (Morse potential)	l_x = 6R, l_y = 6R, l_z = 0.8R
Time step (ps)	0.0015
Temperature (K)	0.01
Plowing velocity (m/s)	36
Plowing depth (α)	0.1~0.8
Plowing direction	[010] on (001) surface

The embedded atom method (EAM) potential [28] is adopted to describe the interactions among copper atoms. We use two types of interaction between asperity pairs to simulate the non-adhesive and adhesive plowing. First, for non-adhesive plowing, the interaction between the asperity pairs is simulated by a repulsive potential with a force of magnitude

$$F_i = \begin{cases} -K(r_i - R)^2, & \text{if } r_i \le R \\ 0, & \text{otherwise} \end{cases}. \quad (7)$$

Here, K is the effective stiffness and set to 10 eV/Å^3 in the simulation. r_i is the distance from the i^{th} atom to the center of rigid asperity. This interaction describes the non-adhesive contact at the interface. Second, for adhesive plowing, the upper asperity was fabricated as a diamond tip which comprises perfect diamond atomic lattices. In the diamond-copper system, the C-C interactions among atoms in the upper asperity are ignored because diamond is much harder than copper. The interaction between asperity pairs is described by the Morse potential as

$$\phi(r) = D_0\left[e^{-2\alpha_0(r-r_0)} - 2e^{-\alpha_0(r-r_0)}\right], \quad (8)$$

where D_0 is cohesion energy, α_0 is elastic modulus, r is the distance between two atoms, and r_0 is the equilibrium distance. Here, these parameters are taken as $D_0 = 0.087$ eV, $\alpha_0 = 5.14$ Å^{-1}, and r_0 = 2.05 Å [46]. To study the effect of interfacial adhesion, we use a factor λ to modify the cohesion energy by $\lambda \cdot D_0$, resulting in different adhesion strengths.

4.2.2 Size independence of plowing wear

Fig. 9(a) presents the effect of asperity size on the final wear volume and the normalized

wear volume V_w/V_a, where V_a is the volume of the undeformed hemispherical asperity and calculated as $2\pi R^3/3$. For the asperity of radius 5a, both the absolute and normalized wear volumes are small due to the limited plastic deformation. For the asperity of radius larger than ~20a, the normalized wear volume exhibits a weak dependence on the asperity size. Therefore, the wear volume can be considered to be proportional to the asperity volume in this case. Fig. 9(b) further confirms the size insensitivity of the normalized wear volume over a wide range of plowing depths for the asperities of radii 20a and 30a.

The distribution of atomic strain for asperities of different sizes is shown in Fig. 9(c); the three asperities are rescaled to have the same dimension in the picture. For the small asperity of radius 10a, only a limited number of atoms at the very top of the asperity are worn. In contrast, for the larger asperities, all atoms on the top region of the asperity are worn, and it is seen that the spatial locations of the worn atoms are almost independent of the asperity size.

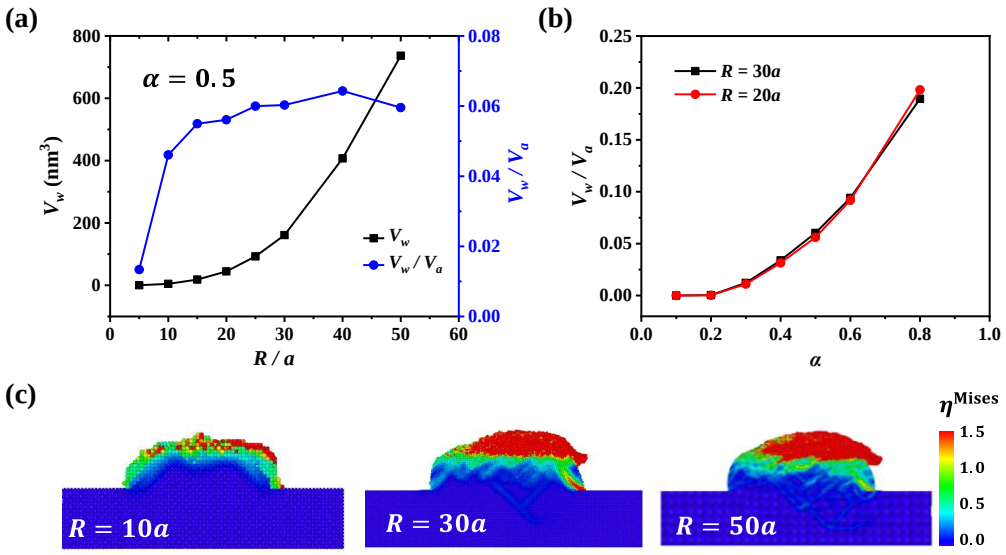

Fig. 9. (a) Effect of the asperity size on the wear volume when $\alpha = 0.5$. (b) The normalized wear volume for two asperities. (c) Distribution of the atomic equivalent strain in the asperity of different sizes when $\alpha = 0.5$. Figures are the cross section of the asperity.

4.2.3 Increased wear rate due to stronger adhesion

The results of non-adhesive plowing for copper asperity of various radii, in terms of Eq. (5), are summarized in Fig. 10. Good linearity can be observed, i.e., k_0 is roughly a constant. Therefore, the Archard wear law is confirmed to be valid for the non-adhesive asperity plowing.

This finding is different from the adhesive wear model due to the flattening and shearing of asperities [10], in which the adhesion is necessary to generate shear loading and then produces asperity wear by plastic deformation. In our model, we confirmed that the Archard wear law still holds in the absence of adhesion.

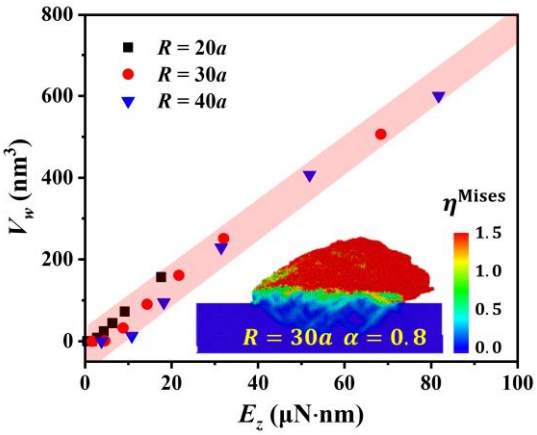

Fig. 10. Wear volume as a function of E_z with k_0 being 7.3 nm^3/(μN·nm). The inset shows the distribution of atomic equivalent strain when $\alpha = 0.8$. The pink shaded region is used to guide the readers for linearity.

For adhesive plowing in the diamond-copper system, the wear law is studied in the asperity of radius $30a$ with two adhesion strengths, i.e., the full adhesion ($\lambda = 1.0$) and the reduced adhesion by $\lambda = 0.5$. As shown in Fig. 11, two clear features can be observed. First, the Archard wear law holds in the adhesive plowing. Second, increasing the adhesion strength results in a higher wear rate k_0. In the insets of Fig. 11, we can see that a small amount of wear is attached to the rigid tip in the case of full adhesion. In contrast, when the adhesion strength is reduced, no debris is attached to the tip. Despite the difference, the wear processes with and without adhesion discussed above can be attributed to the same wear mechanism: wear is essentially dominated by plasticity-induced asperity smoothing [9]. In this situation, the Archard law always holds for copper.

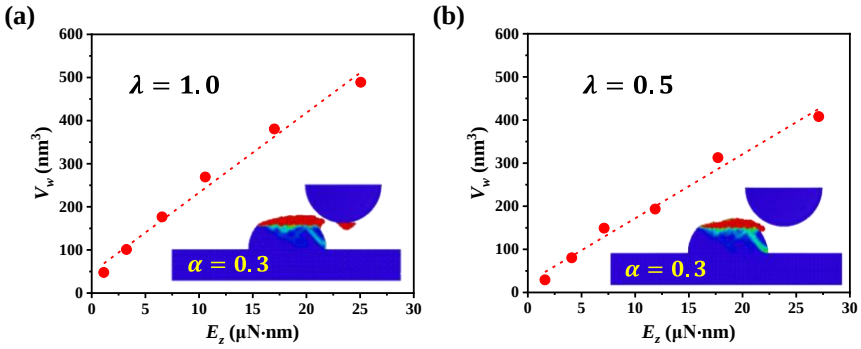

Fig. 11. Wear volume as a function of E_z: (a) full adhesion ($\lambda = 1.0$) with k_0 being 18.5 nm^3/(μN·nm); (b) $\lambda = 0.5$ with k_0 being 14.8 nm^3/(μN·nm). The inset shows the strain distribution following the color scheme in Fig. 10.

5. Conclusions

In this paper, through MD simulations of plowing wear in asperities using coarse-grained interatomic potentials and real material potentials, we addressed the fundamental question: whether Archard wear law holds for interlocking asperities. The main findings are summarized as follows:

1) There exists a critical asperity size below which the wear is dominated by the plastic deformation, and thus Archard wear law holds. The Archard wear law breaks down when the wear is dominated by the formation of fractured debris during plowing.

2) Increasing the material ductility or decreasing the interfacial adhesion makes the wear mechanism easier to transform from fracture-induced debris to plasticity-induced smoothing. Increasing initial dislocations may lead to a larger critical size of asperity due to the increased ductility.

3) An equation of the critical asperity size for the formation of fractured debris is proposed. The critical asperity size is estimated to be on the length scale of hundred nanometers for pristine crystals and several micron meters to hundred micron meters for crystals with initial defects. For ductile materials like copper, we confirmed by MD simulation that the Archard wear law maintains validity in both non-adhesive and adhesive plowing.

Appendix A: Coarse-grained interatomic potentials

This appendix introduced the coarse-grained interatomic potentials. As mentioned in [9],

the material ductility can be modified by changing the tail of a Morse potential. In detail, the modified Morse potentials are developed as follows:

$$\frac{E(r)}{\varepsilon} = \begin{cases} e^{-2\alpha_0(r-r_0)} - 2e^{-\alpha_0(r-r_0)} & r < 1.1r_0 \\ a_3r^3 + a_2r^2 + a_1r^1 + a_0 & 1.1r_0 \le r < r_c \\ 0 & r_c \le r \end{cases}. \quad (9)$$

Here, $E(r)$ is the potential energy between two atoms with distance r. ε is the depth of the potential well and is 1.0, and r_0 is the equilibrium bond distance. α_0 governs the bond stiffness and is equal to $7.3r_0^{-1}$. The truncation at $1.1r_0$ ensures the elastic properties unchanged up to 10% strain. The r_c is a parameter that governs the tail of interatomic potentials and then controls the unstable stacking fault energy. The parameters $a_0 \sim a_3$ ensure the continuity of the bond energy and the force.

In this study, we constructed three sets of potentials, as shown in Fig. A1(a). The potential with a shorter cut-off radius ($r_c = 1.22r_0$) corresponds to a more brittle material. In contrast, the increase of cut-off radius (e.g., $r_c = 1.38r_0$) makes the material more ductile. Therefore, using these model potentials, we essentially studied the wear law in different material systems. All the models with modified Morse potentials are constructed in the FCC structure with the lattice constant a being $\sqrt{2}r_0$. The Young's modulus for all materials is $150\varepsilon r_0^{-3}$ [27]. The indentation is simulated at the temperature of $0.005\,\varepsilon/k_B$ for materials with the modified Morse potentials, and the results are shown in Fig. C1(b). The material hardness is calculated by averaging the contact stresses at the normalized indentation depth between 0.3 and 0.4. More details for the hardness of indentation and flattening are given in the Supplementary Material. Generally, a more brittle material has a larger hardness in this model.

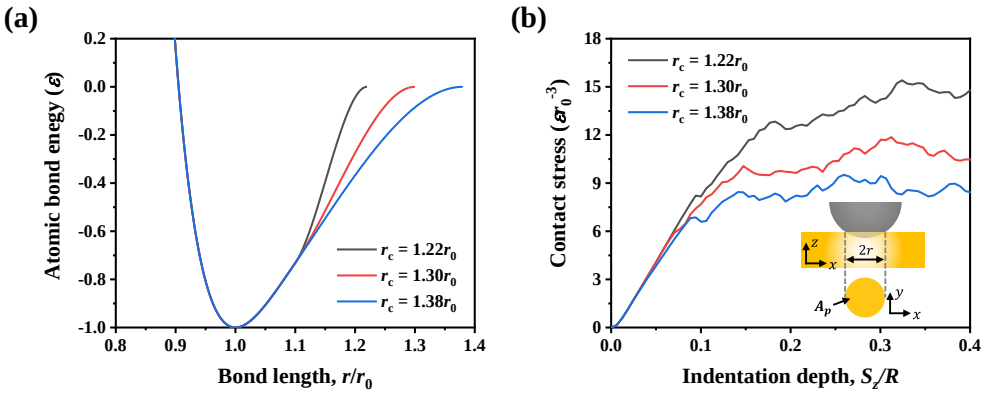

Fig. A1. (a) The bond energy versus atomic bond length for different cut-off radius r_c. (b)

Contact stress for materials with potentials of different r_c; the inset shows the indentation model with an indenter of radius 30a.

Appendix B: Determination of wear volume

In this appendix, we proposed a new method to evaluate the wear volume during asperity plowing. Nano-scratching simulations on an atomically smooth copper substrate are carried out as the benchmark. The nano-scratching model consists of a rigid indenter with a radius of 5 nm and a copper substrate of dimensions $\sim 30 \times 30 \times 10$ nm^3, see inset in Fig. A1. We used the same repulsive potential (Eq. (7)) as in the simulation of non-adhesive plowing to describe the interaction between the indenter and the substrate. The simple geometry in this model allows us to utilize a simple conventional criterion/definition of worn atoms: atoms on the top of the original substrate surface. The wear volume evaluated by the simple conventional criterion serves as a reference for developing the new wear criterion using the atomic equivalent strain η^{Mises} [21]. The atomic equivalent strain η^{Mises} is defined as

$$\eta^{\mathrm{Mises}} = \sqrt{\eta_{yz}^2 + \eta_{xz}^2 + \eta_{xy}^2 + \frac{(\eta_{yy}-\eta_{zz})^2+(\eta_{xx}-\eta_{zz})^2+(\eta_{xx}-\eta_{yy})^2}{6}}, \quad (10)$$

where η_{ij} is the component the strain tensor defined as $\boldsymbol{\eta} = \frac{1}{2}(\boldsymbol{JJ^T} - \boldsymbol{I})$, $\boldsymbol{J}$ is the local deformation gradient which is calculated based on the reference atomic configuration at the initial moment of sliding, and $\boldsymbol{I}$ is the unit tensor.

As shown in Fig. B1, we first obtain the worn atoms by the conventional criterion in two different scratching depths; in both cases, the wear volume increases with the increasing scratching distance. We then calculate the volume of the worn atoms using different atomic equivalent strains as the threshold. By comparing the wear volume defined by the two methods, the atomic equivalent strain of 1.5 is calibrated as the criterion of worn atoms. For nano scratching using a hemispherical diamond tip on the copper substrate where adhesion exists, we repeated the above calibration process, and it was found that the atomic equivalent strain of 1.5 is also the threshold strain.

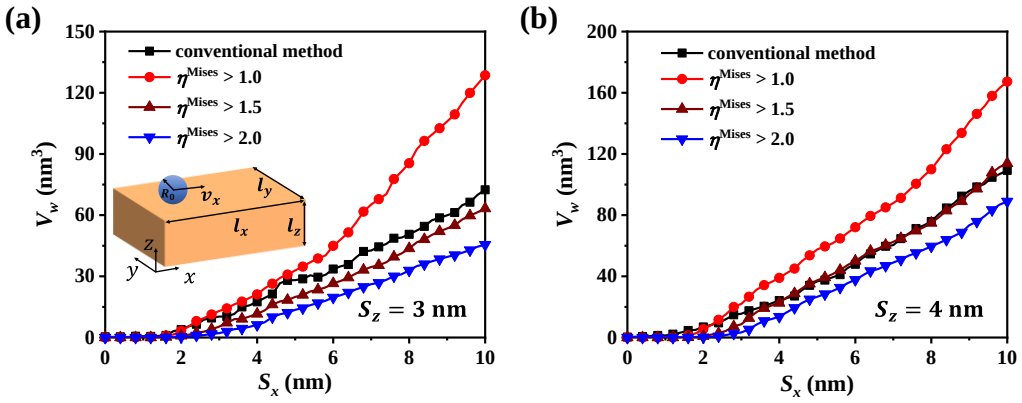

Fig. B1. Evaluation of the wear volume using different atomic equivalent strains as the threshold when the scratching depths are (a) $S_z = 3$ nm and (b) $S_z = 4$ nm. The inset in (a) illustrates the nano-scratching model.

Using the above method, we can also determine the wear criterion for the materials of coarse-grained potentials. We evaluated the wear volume at two scratching depths and determined the threshold strain for each potential, and the results for the material of $r_c = 1.38r_0$ are shown in Fig. B2. The threshold strains for the worn atoms are 6.0, 4.0, and 3.0 for the materials of $r_c = 1.22r_0$, $r_c = 1.30r_0$, and $r_c = 1.38r_0$, respectively. It can be seen that the calibrated threshold strains are different for materials of different ductility.

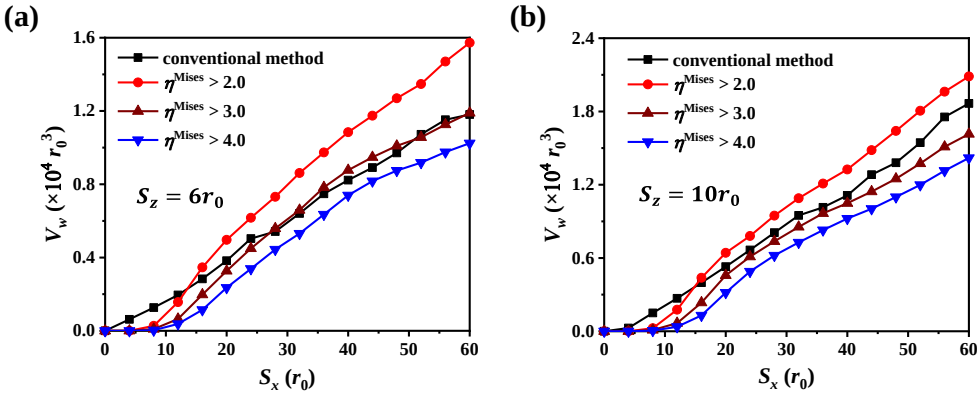

Fig. B2. Evaluation of the wear volume using different atomic equivalent strains as the threshold in material of $r_c = 1.38r_0$ when the scratching depths are (a) $S_z = 6r_0$ and (b) $S_z = 10r_0$.

Appendix C: Determination of plastic smoothing or fractured debris

For the asperity plowing, the asperity wear could originate from two different mechanisms,

i.e., the plasticity-induced asperity smoothing and the fractured wear debris. In the simulation, the formation of fractured wear debris is also accompanied by a large amount of plasticity. Therefore, it is crucial to have a criterion that determines which mechanism dominates the wear process. Here, a criterion is developed based on the formation of the new free surface: we first calculated the increase of the area of free surface ΔS by the analysis of construct surface mesh [47] when the plowing is finished, and then normalized the area ΔS by $2\pi R^2$ to calculate a dimensionless ratio η_f, i.e., $\eta_f = \Delta S/2\pi R^2$.

As shown in Fig. C1, good linearity can be observed between η_f and the normalized plowing depth α. For many data points that satisfy the observed linear relationship, we are sure that the wear mechanism is plasticity (from the deformed asperity topology); therefore, we believe that this linearity can be used as the criterion of plasticity dominated wear. For brittle asperity of radius larger than 30a, the η_f deviates from the linear relation due to the more significant increase of free surface generated by the asperity fracture. In this study, the plowing wear is considered to be fracture-dominated when $(\eta_f - \eta_0)/\eta_0 > 0.2$.

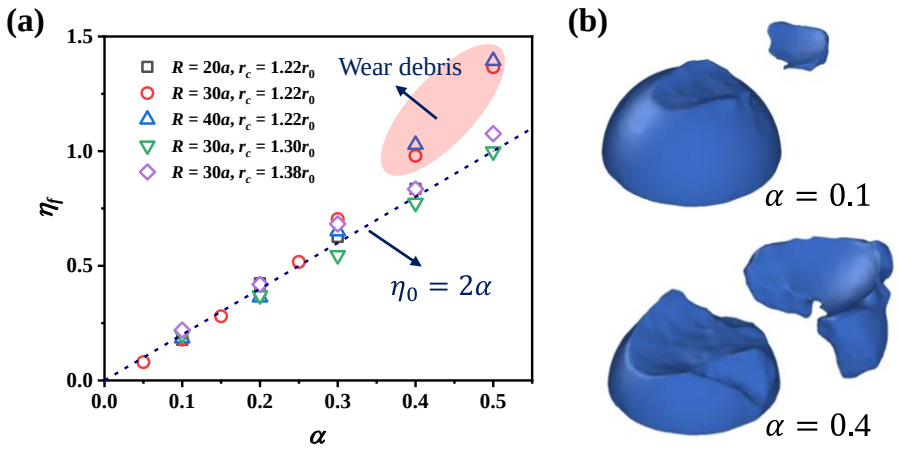

Fig. C1. (a) Increase of free surface in asperities due to plowing wear. (b) Illustration of two wear configurations in asperity with $r_c = 1.22r_0$ at different plowing depths, and the asperity radius is 30a.

Acknowledgement

This work was supported by the National Natural Science Foundation of China, Basic Science Center Program for "Multiscale Problems in Nonlinear Mechanics" (No.11988102), by

the National Natural Science Foundation of China (12172358, 11972347, 12022210, 12032001), and by Youth Innovation Promotion Association CAS (2018022).

CRediT authorship contribution statement

Jianqiao Hu: Conceptualization, Methodology, Investigation, Formal analysis, Writing-original draft. **Hengxu Song**: Conceptualization, Validation, Data curation, Project administration, Writing-review & editing. **Stefan Sandfeld**: Writing - review & editing, Funding acquisition. **Xiaoming Liu:** Project administration, Conceptualization, Writing-review & editing, Supervision, Funding acquisition. **Yueguang Wei**: Supervision, Resources.

Declaration of competing interest

The authors declare that they have no known competing financial interests or personal relationships that could have appeared to influence the work reported in this paper.

References

[1] K. Holmberg, A. Erdemir, Influence of tribology on global energy consumption, costs and emissions. Friction 2017; 5(3): 263-284.

[2] J.F. Archard, Contact and rubbing of flat surfaces. Journal of Applied Physics 1953; 24(8): 981-988.

[3] J.F. Archard, W. Hirst, The wear of metals under unlubricated conditions. Proceedings of the Royal Society of London. Series A. Mathematical and Physical Sciences 1997; 236(1206): 397-410.

[4] S.M. Hsu, M.C. Shen, A.W. Ruff, Wear prediction for metals. Tribology International 1997; 30(5): 377-383.

[5] M.Z. Huq, J.P. Celis, Expressing wear rate in sliding contacts based on dissipated energy. Wear 2002; 252(5-6): 375-383.

[6] J. Yan, A. Lindo, R. Schwaiger, A.M. Hodge, Sliding wear behavior of fully nanotwinned Cu alloys. Friction 2018; 7(3): 260-267.

[7] B. Bhushan, S. Sundararajan, Micro/nanoscale friction and wear mechanisms of thin films using atomic force and friction force microscopy. Acta Materialia 1998; 46(11): 3793-3804.

[8] K.-H. Chung, D.-E. Kim, Fundamental investigation of micro wear rate using an atomic force microscope. Tribology Letters 2003; 15(2): 135-144.

[9] R. Aghababaei, D.H. Warner, J.F. Molinari, Critical length scale controls adhesive wear mechanisms. Nature communications 2016; 7: 11816.

[10] K. Zhao, R. Aghababaei, Adhesive wear law at the single asperity level. Journal of the Mechanics and Physics of Solids 2020; 143: 104069.

[11] K. Zhao, R. Aghababaei, Interfacial plasticity controls material removal rate during adhesive sliding contact. Physical Review Materials 2020; 4(10): 103605.

[12] Y. Yang, L. Huang, Y. Shi, Adhesion suppresses atomic wear in single-asperity sliding. Wear 2016; 352-353: 31-41.

[13] Y. Yang, Y. Shi, Single asperity friction in the wear regime. Friction 2018; 6(3): 316-322.

[14] H. Song, H. Yavas, E.V.d. Giessen, S. Papanikolaou, Discrete dislocation dynamics simulations of nanoindentation with pre-stress: Hardness and statistics of abrupt plastic events. Journal of the Mechanics and Physics of Solids 2019; 123: 332-347.

[15] R. Aghababaei, K. Zhao, Micromechanics of material detachment during adhesive wear: a numerical assessment of Archard's wear model. Wear 2021; 476: 203739.

[16] S. Plimpton, Fast parallel algorithms for short-range molecular dynamics. Journal of Computational Physics 1995; 117(1): 1-19.

[17] A. Stukowski, K. Albe, Extracting dislocations and non-dislocation crystal defects from atomistic simulation data. Modelling and Simulation in Materials Science and Engineering 2010; 18(8): 085001.

[18] A. Stukowski, Visualization and analysis of atomistic simulation data with OVITO–the open visualization tool. Modelling and Simulation in Materials Science and Engineering 2010; 18(1): 015012.

[19] P. Zhu, R. Li, H. Gong, Molecular dynamics simulation of nanoscale abrasive wear of polycrystalline silicon. Crystals 2018; 8(12): 463.

[20] A. Li, I. Szlufarska, How grain size controls friction and wear in nanocrystalline metals. Physical Review B 2015; 92(7): 075418.

[21] F. Shimizu, S. Ogata, J. Li, Theory of shear banding in metallic glasses and molecular

dynamics calculations. Materials Transactions 2007; 48(11): 2923-2927.

[22] J. Hu, F. Yuan, X. Liu, Y. Wei, Effect of plasticity on nanoscale wear of third-body particles. Tribology International 2021; 155: 106739.

[23] J. Zhong, J.B. Adams, L.G. Hector, Molecular dynamics simulations of asperity shear in aluminum. Journal of Applied Physics 2003; 94(7): 4306-4314.

[24] J. Zhong, R. Shakiba, J.B. Adams, Molecular dynamics simulation of severe adhesive wear on a rough aluminum substrate. Journal of Physics D: Applied Physics 2013; 46(5): 055307.

[25] I. Hutchings, M. Gee, E. Santner, Friction and Wear. Springer Handbook of Materials Measurement Methods 2006: 685-710.

[26] H. Song, V.S. Deshpande, E. Van der Giessen, Discrete dislocation plasticity analysis of loading rate-dependent static friction. Proceedings of the Royal Society A: Mathematical, Physical and Engineering Sciences 2016; 472(2192): 20150877.

[27] R. Aghababaei, On the origins of third-body particle formation during adhesive wear. Wear 2019; 426-427: 1076-1081.

[28] Y. Mishin, M.J. Mehl, D.A. Papaconstantopoulos, A.F. Voter, J.D. Kress, Structural stability and lattice defects in copper:Ab initio, tight-binding, and embedded-atom calculations. Physical Review B 2001; 63(22): 224106.

[29] S. Foiles, M. Baskes, M. Daw, Embedded-atom-method functions for the FCC metals Cu, Ag, Au, Ni, Pd, Pt, and their alloys. Physical Review B 1986; 33(12): 7983-7991.

[30] F.H. Stillinger, T.A. Weber, Computer simulation of local order in condensed phases of silicon. Phys Rev B Condens Matter 1985; 31(8): 5262-5271.

[31] D. Kiener, A.M. Minor, Source-controlled yield and hardening of Cu(100) studied by in situ transmission electron microscopy. Acta Materialia 2011; 59(4): 1328-1337.

[32] Z. Wang, Z. Shan, J. Li, J. Sun, E. Ma, Pristine-to-pristine regime of plastic deformation in submicron-sized single crystal gold particles. Acta Materialia 2012; 60(3): 1368-1377.

[33] C.P. Frick, B.G. Clark, S. Orso, A.S. Schneider, E. Arzt, Size effect on strength and strain hardening of small-scale [111] nickel compression pillars. Materials Science and Engineering: A 2008; 489(1-2): 319-329.

[34] M.S. Colla, B. Wang, H. Idrissi, D. Schryvers, J.P. Raskin, T. Pardoen, High strength-

ductility of thin nanocrystalline palladium films with nanoscale twins: On-chip testing and grain aggregate model. Acta Materialia 2012; 60(4): 1795-1806.

[35] K.N. Jonnalagadda, I. Chasiotis, S. Yagnamurthy, J. Lambros, J. Pulskamp, R. Polcawich, M. Dubey, Experimental Investigation of Strain Rate Dependence of Nanocrystalline Pt Films. Experimental Mechanics 2009; 50(1): 25-35.

[36] M. Chen, L. Petho, A.S. Sologubenko, H. Ma, J. Michler, R. Spolenak, J.M. Wheeler, Achieving micron-scale plasticity and theoretical strength in Silicon. Nature communications 2020; 11(1): 2681.

[37] A. Chauniyal, G. Dehm, R. Janisch, On the role of pre-existing defects in influencing hardness in nanoscale indentations — Insights from atomistic simulations. Journal of the Mechanics and Physics of Solids 2021; 154: 104511.

[38] J. Hu, X. Ye, X. Liu, Z. Chen, The effects of initial void and dislocation on the onset of plasticity in copper single crystals. Journal of Applied Physics 2019; 126(16): 165104.

[39] R.-G. Xu, H. Song, Y. Leng, S. Papanikolaou, A molecular dynamics simulations study of the influence of prestrain on the pop-In behavior and indentation size effect in Cu single crystals. Materials 2021; 14(18): 5220.

[40] M. Mishra, I. Szlufarska, Dislocation controlled wear in single crystal silicon carbide. Journal of Materials Science 2012; 48(4): 1593-1603.

[41] J. Sun, L. Fang, J. Han, Y. Han, H. Chen, K. Sun, Abrasive wear of nanoscale single crystal silicon. Wear 2013; 307(1-2): 119-126.

[42] J. Hu, H. Song, Z. Liu, Z. Zhuang, X. Liu, S. Sandfeld, Predicting the flow stress and dominant yielding mechanisms: analytical models based on discrete dislocation plasticity. Scientific reports 2019; 9(1): 20422.

[43] S. Papanikolaou, H. Song, E. Van der Giessen, Obstacles and sources in dislocation dynamics: Strengthening and statistics of abrupt plastic events in nanopillar compression. Journal of the Mechanics and Physics of Solids 2017; 102: 17-29.

[44] H. Song, R.J. Dikken, L. Nicola, V.D.E. Giessen, Plastic ploughing of a sinusoidal asperity on a rough surface. Journal of Applied Mechanics 2015; 82(7): 071006.

[45] H. Song, S. Papanikolaou, From statistical correlations to stochasticity and size effects in

sub-micron crystal plasticity. Metals 2019; 9(8): 835.

[46] P. Zhu, Y. Hu, T. Ma, H. Wang, Study of AFM-based nanometric cutting process using molecular dynamics. Applied Surface Science 2010; 256(23): 7160-7165.

[47] A. Stukowski, Computational analysis methods in atomistic modeling of crystals. JOM 2013; 66(3): 399-407.